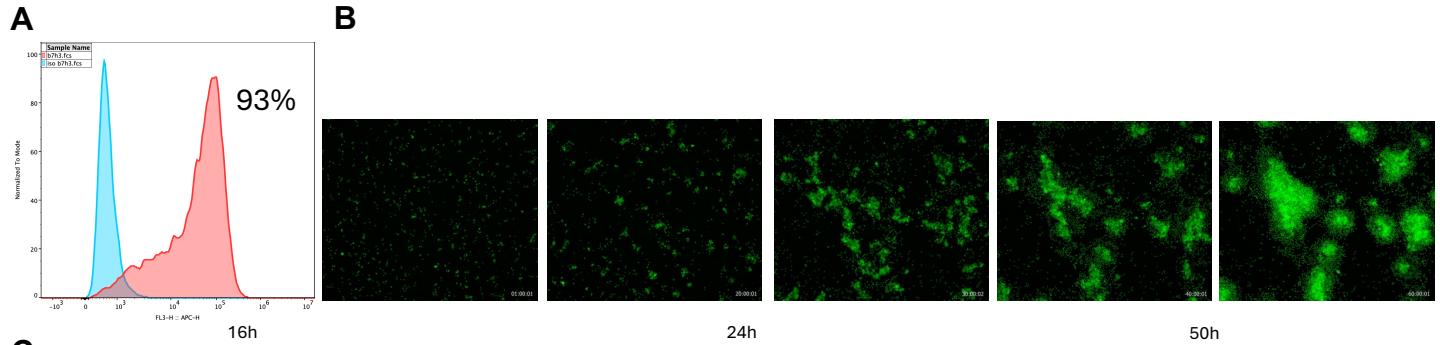

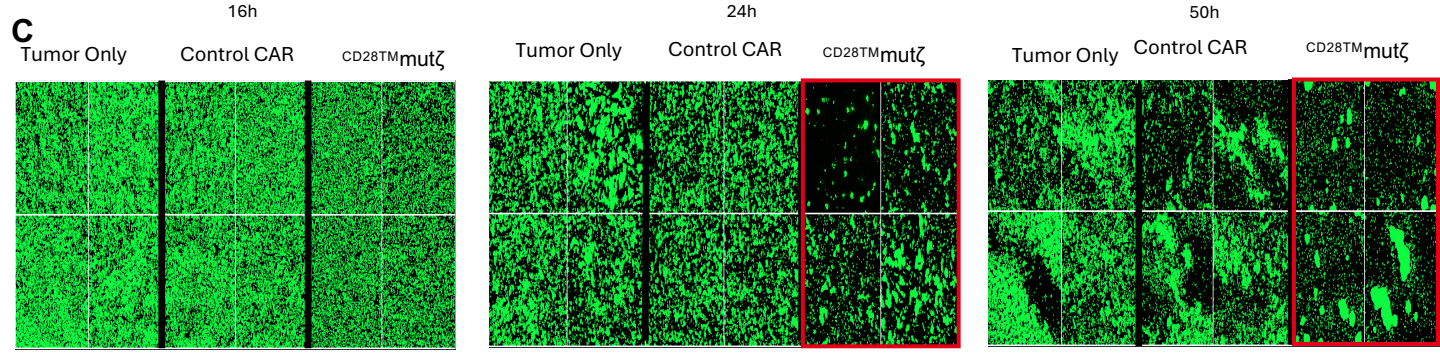

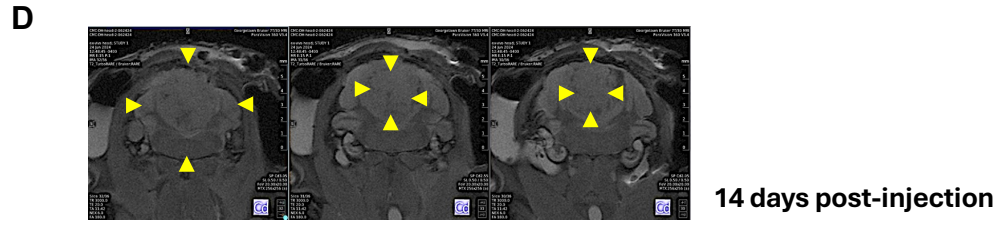

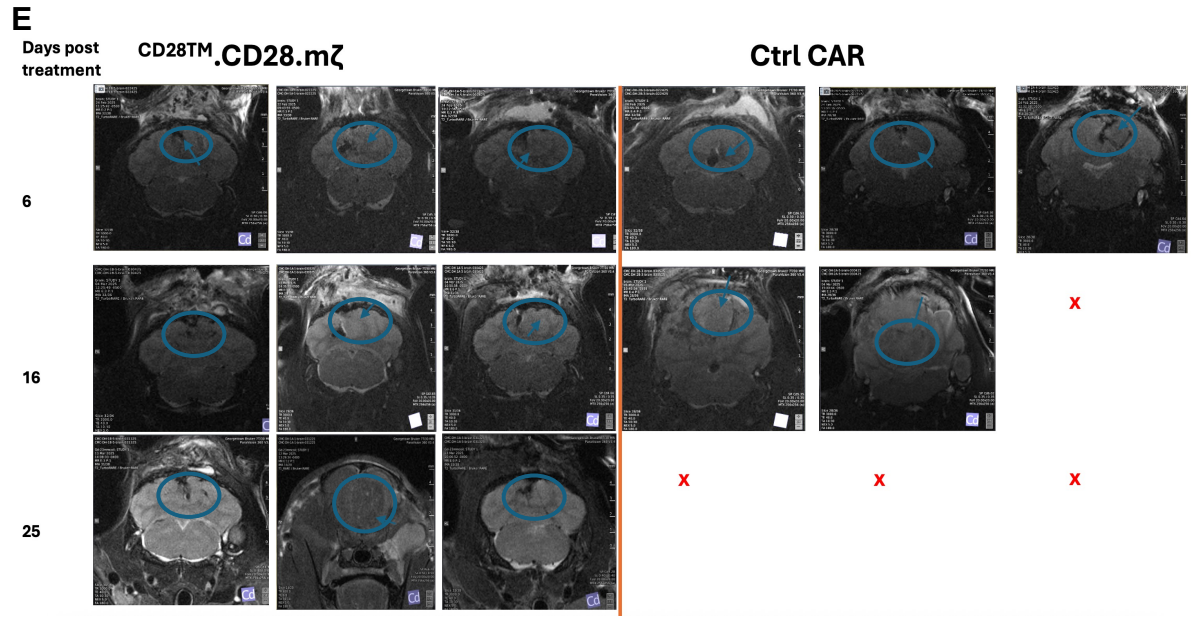

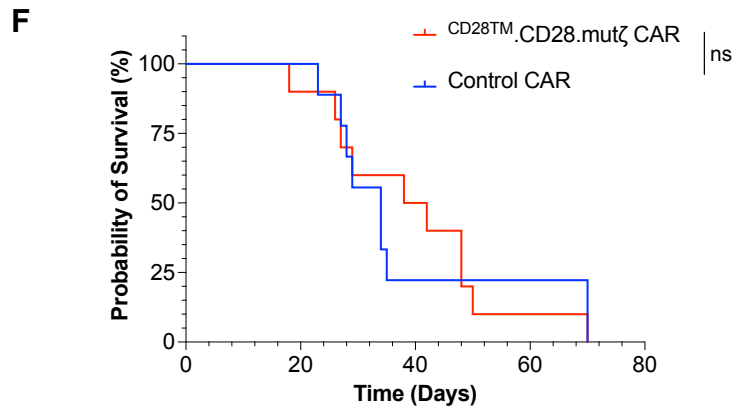

Supplementary Figure 1

Supplementary Figure S1. Functional potency of murine ^{CD28TM}mζ CAR T cells against B7-H3 enriched 1232 G3MB murine tumor model

A. Flow cytometry-based verification of B7-H3 expression in 1232 G3MB murine tumor model – 93% expression

B. Representative sequential live-cell fluorescence images of 1232 tumor cells acquired during xCELLigence imaging using Agilent ELive Green dye. Serial snapshots demonstrate temporal changes in tumor cell growth and clustering, with green fluorescence indicating viable cells

C. Real-time cytotoxicity assay using the xCELLigence platform. Tumor cells were plated and CAR T cells added at a 2:1 E:T ratio. Etox green, a fluorescent live-cell stain, was added upon tumor cell plating. Cytotoxicity was quantified visually. Differential cytotoxicity exhibited between control CAR and fully-functional standard B7-H3 CAR harboring CD28 transmembrane and costimulatory domains. Imaging portrayed is shown at 16 hours (no CAR T cells added), followed by CAR-T cells added in culture at 24 & 50 hours.

D. Representative MRI images confirming establishment of orthotopic G3MB tumors in immunocompetent mice at 14 days post-implantation. Arrowheads indicate cerebellar tumor burden at the time of treatment initiation.

E. In vivo testing of the CAR design previously shown to be active in glioma models. C57BL/6 mice bearing orthotopic Group 3 medulloblastoma tumors received 2×10^6 intratumoral murine CAR T cells on day 14 after cerebellar implantation, and tumor burden was monitored by longitudinal MRI. Representative images show initial tumor control with the CD28-based CAR, but no durable suppression of tumor growth, whereas control CAR-treated mice demonstrated more rapid progression.

F. Kaplan–Meier survival analysis revealed no significant survival benefit with CD28-based CAR T-cell treatment relative to control CAR treatment (n = 10 per group).

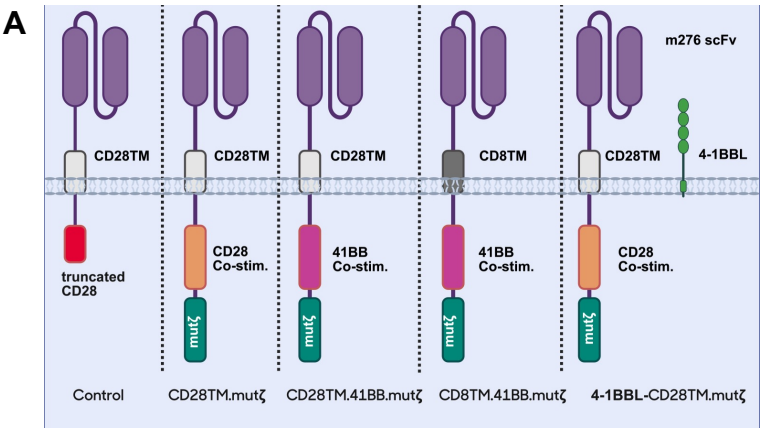

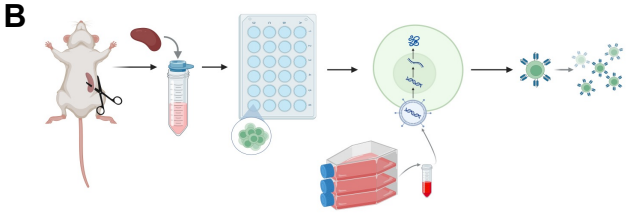

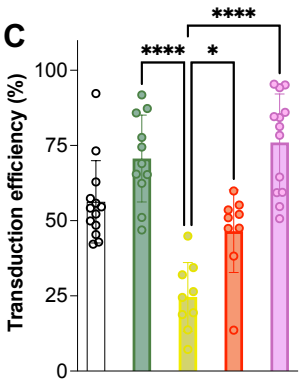

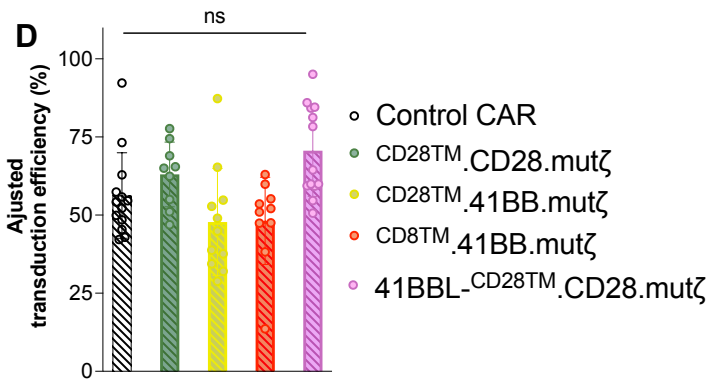

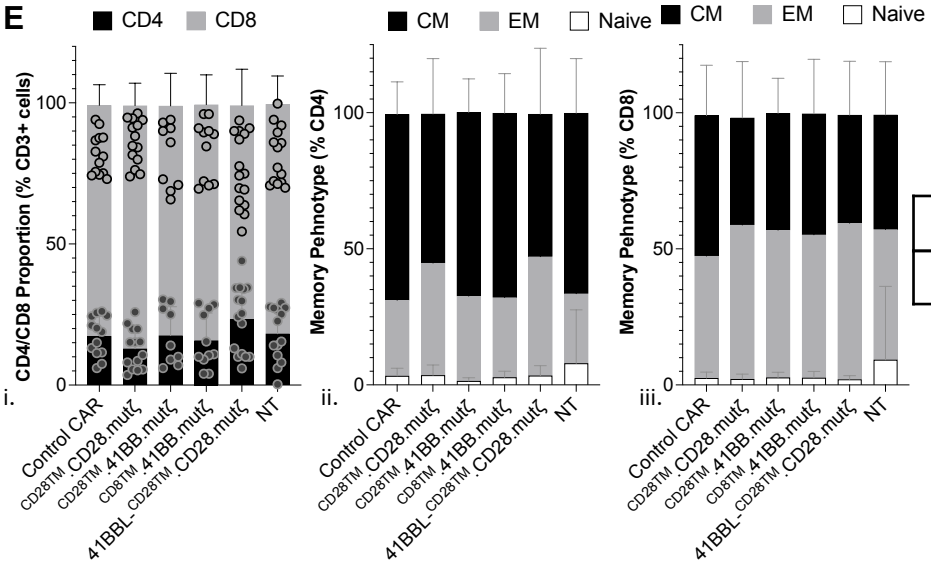

CD28TMmutζ vs. 41BBLCD28TMmutζ	CD4	0.0498
NT vs. 41BBLCD28TMmutζ	CD4 EM	0.0234

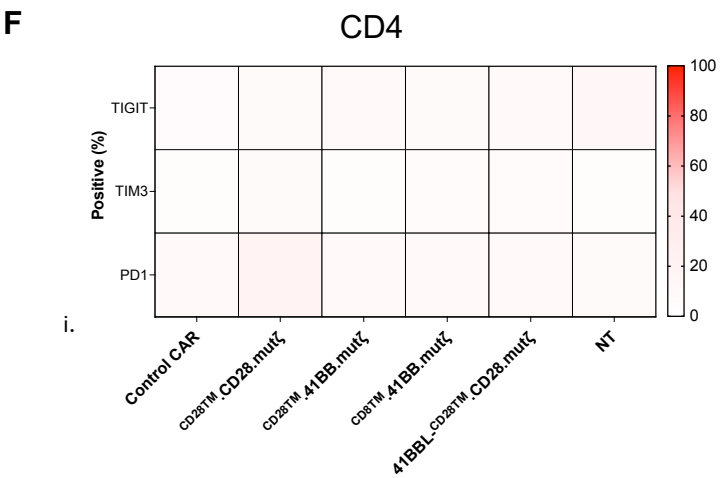

Control (PD1-CD4)	CD28TM.CD28.mutζ (PD1-CD4)	p=0.0217
Control (PD1-CD8)	CD28TM.CD28.mutζ (PD1-CD8)	p=0.0433

Supplementary Figure 2

Supplementary Figure S2. Generation and characterization of murine B7-H3 CAR T cells with distinct CAR designs.

A. Diagram exhibiting murine CAR-T cell panel targeting B7-H3. *Created in BioRender. Yaacoub, S. (2026) https://BioRender.com/baospw2*

B. CAR transduction protocol workflow. Created in BioRender. Yaacoub, S. (2026) https://BioRender.com/82w37nf

C. CAR expression in murine T cells was assessed by flow cytometry using a Fab fragment specific to the scFv region of each CAR construct. Non-transduced (NT) T cells served as controls. Constructs showed differential transduction (n = 6–12 per construct; mean ± SEM; two-way ANOVA with Tukey's multiple comparisons test)

D. Estimated modified transduction efficiencies of CAR T cells after dilution with NT cells to achieve more comparable rates.

E. Summary of CD4 and CD8 T cell composition in mB7-H3 CAR T cell products at day 5 post-transduction (n = 11; mean ± SEM; two-way ANOVA with Tukey's test) (i). Memory phenotype distribution of CD4 (ii) and CD8 (iii) T cells in mB7-H3 CAR products, categorized as effector memory (EM: $CD44^+/CD62L^-$), central memory (CM: $CD44^+/CD62L^+$), and naïve (N: $CD44^-/CD62L^+$) (n = 11; mean ± SEM; two-way ANOVA with Tukey's test).

F. Heatmaps showing surface expression levels of three exhaustion markers in CD4 (i) and CD8 (ii) T cells.

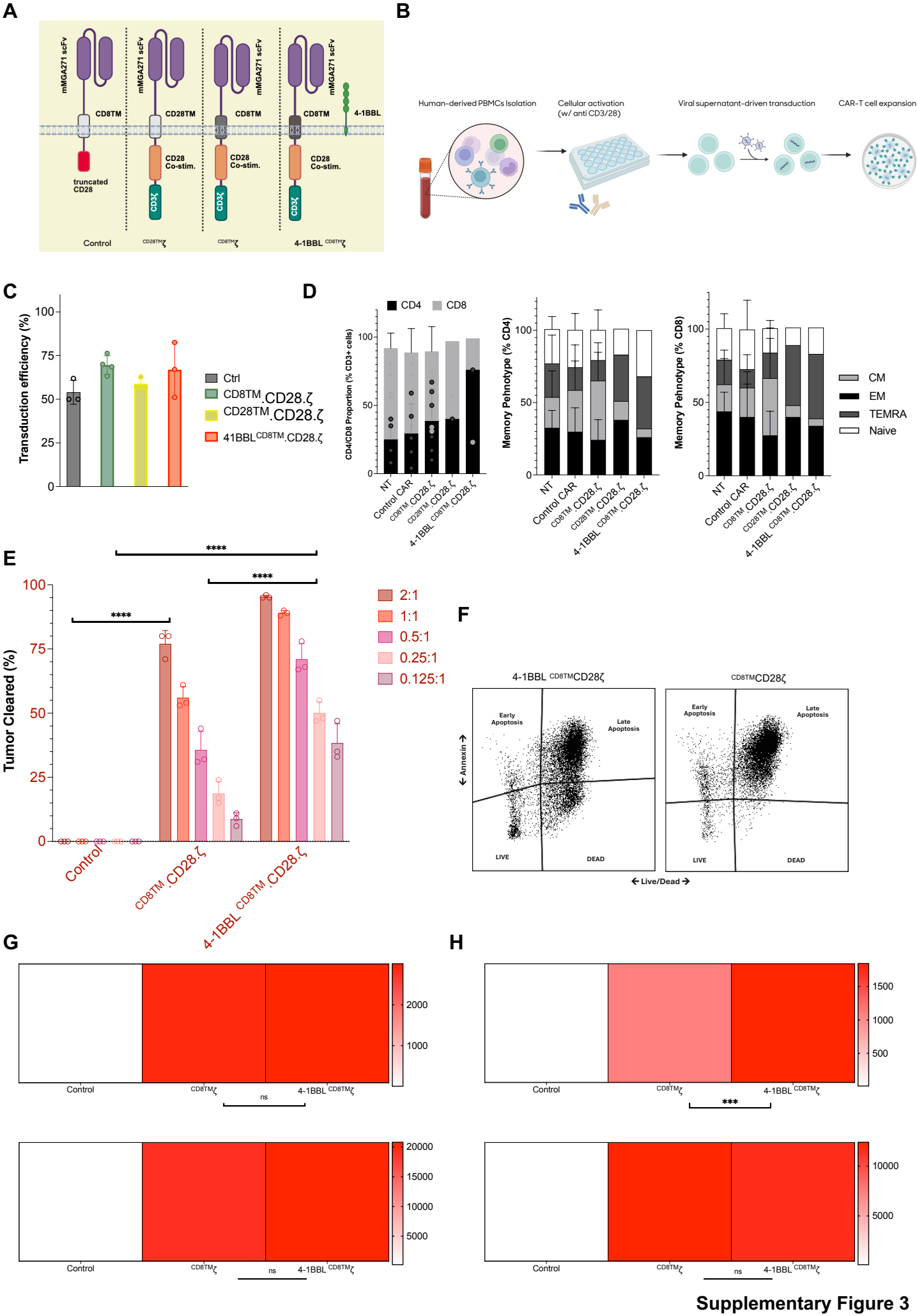

Supplementary Figure 3

Supplementary Figure S3. Generation and in vitro functional characterization of human CAR T-cell constructs incorporating distinct co-stimulatory configurations.

A. Schematic representation of the CAR constructs used in this study, including the control and indicated CAR designs with CD8/28 transmembrane and CD3ζ signaling components, with additional co-stimulatory elements. *Created in BioRender. Yaacoub, S. (2026)* https://BioRender.com/imsk5l9

B. Transduction workflow of human CAR T cells from PBMCs, including PBMC isolation, anti-CD3/CD28-mediated activation, viral supernatant-driven transduction, and ex vivo expansion. *Created in BioRender. Yaacoub, S. (2026)* https://BioRender.com/8yre8j3

C. Transduction efficiency for the indicated constructs, shown as the percentage of marker-positive cells following viral transduction. CAR expression in human-derived CAR-T cells was assessed by flow cytometry using a Fab fragment specific to the scFv region of each CAR construct. Non-transduced (NT) T cells served as controls. All constructs showed efficient transduction

D. Phenotypic distribution of CAR T-cell subsets across constructs, including CD4/CD8 composition (i) and differentiation states (CD4-ii;CD8-iii) as defined by naïve, central memory, effector memory, and terminal effector/effector-like compartments. These data show broadly comparable manufacturing characteristics across constructs with differences in subset distribution depending on CAR design.

E. Cytotoxicity index assay of the indicated CAR T-cell products against target G3MB (D556.ffluc) tumor cells at the specified effector-to-target ratios, demonstrating enhanced tumor cell killing by effector CAR-engineered cells relative to control CAR conditions, with greater killing potential at higher CAR-Tumor ratios.

F. Representative flow cytometric plots of annexin assays conducted on CAR-T cells against suspension G3MB tumor models, specifically MB002.ffluc. The flow plots delineate quadrants representing live, early apoptotic, late apoptotic, and dead populations.

G. Heatmap-style summary of secreted cytokine concentrations derived from co-culture assays against D556.ffluc:
i- IL-2
ii – IFN-y

H. Heatmap-style summary of secreted cytokine concentrations derived from co-culture assays against MB002.ffluc:
i- IL-2
ii – IFN-y

A

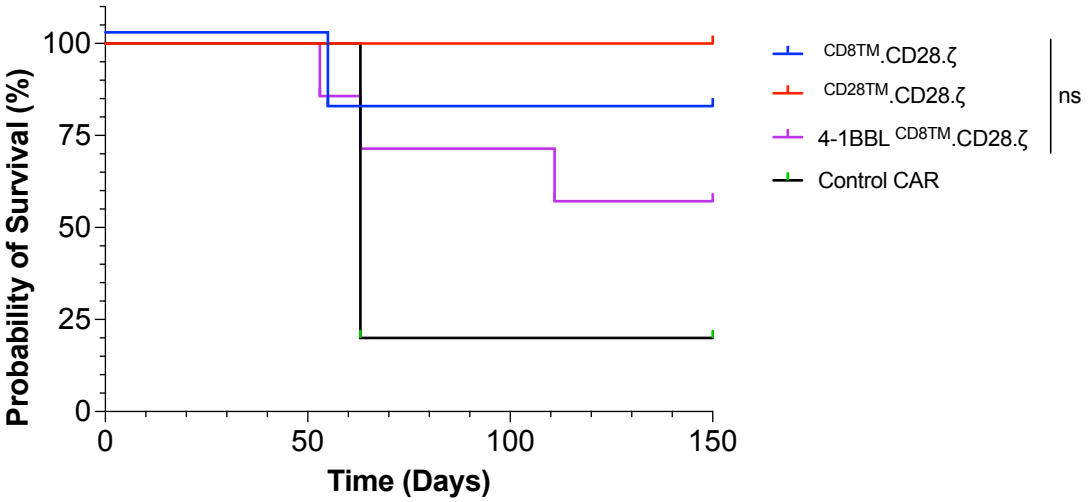

B

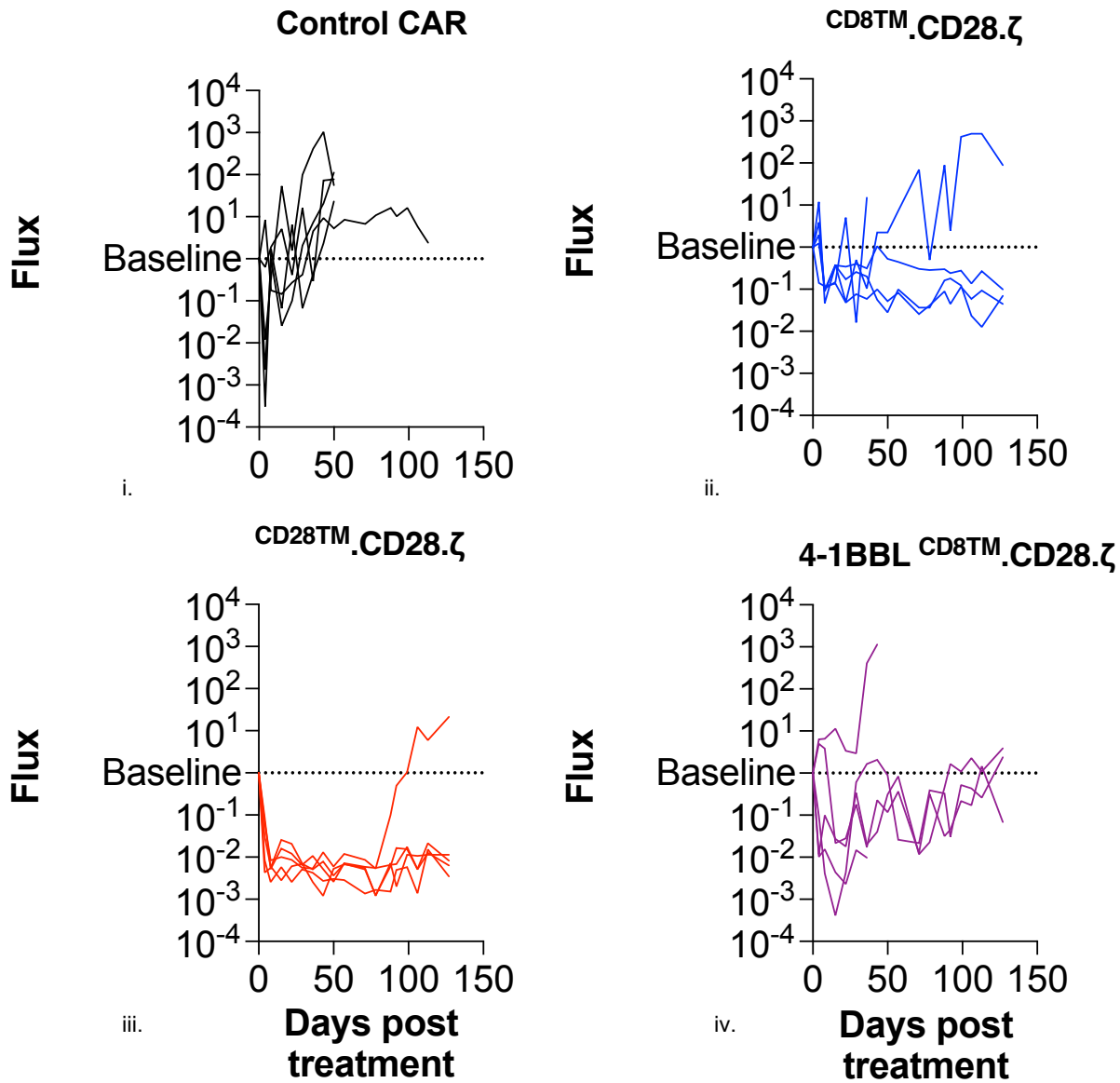

Supplementary Figure 4

Supplementary Figure S4. Human-based B7-H3 CAR-T cell in vivo study in immunodeficient NSG mice with D556.FFLUC

A. Kaplan–Meier survival curves demonstrating broadly comparable survival across mice treated with the indicated human CAR T-cell constructs, with no significant differences between groups.

B. Longitudinal bioluminescence analysis showing fold change in flux after treatment for individual mice in each CAR group. These plots delineate relative tumor burden over time and highlight construct-dependent differences in tumor control. Control CARs noticeably did not control tumor burden post treatment.

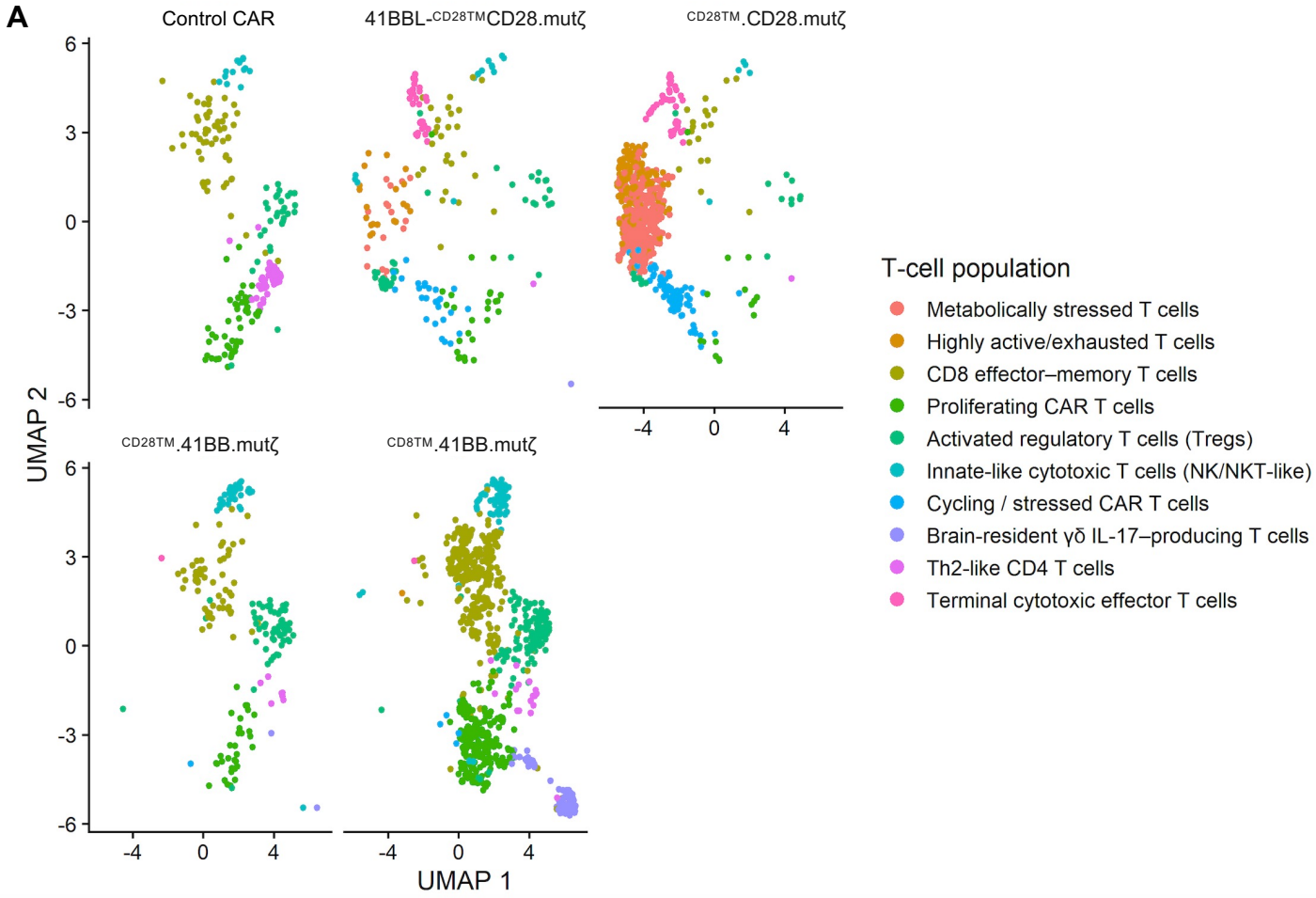

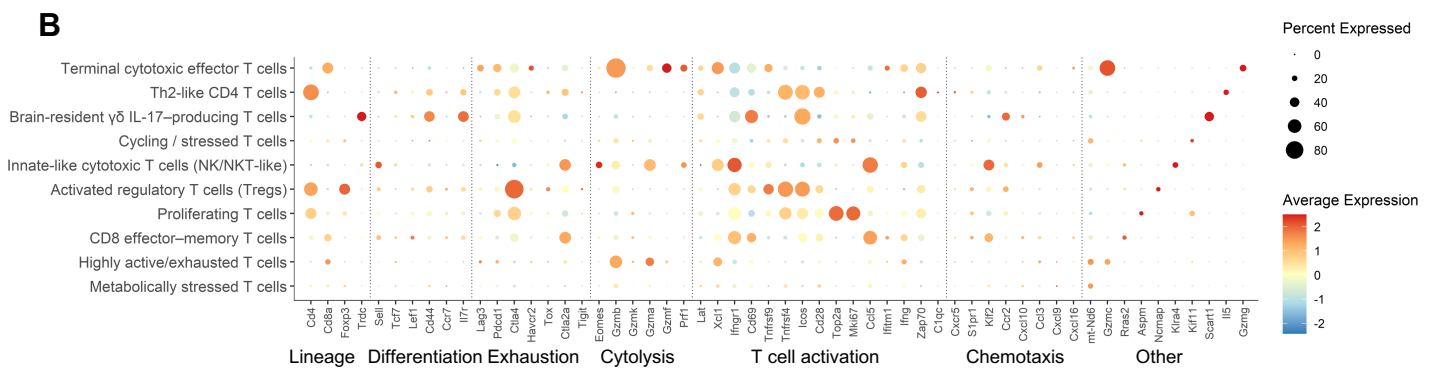

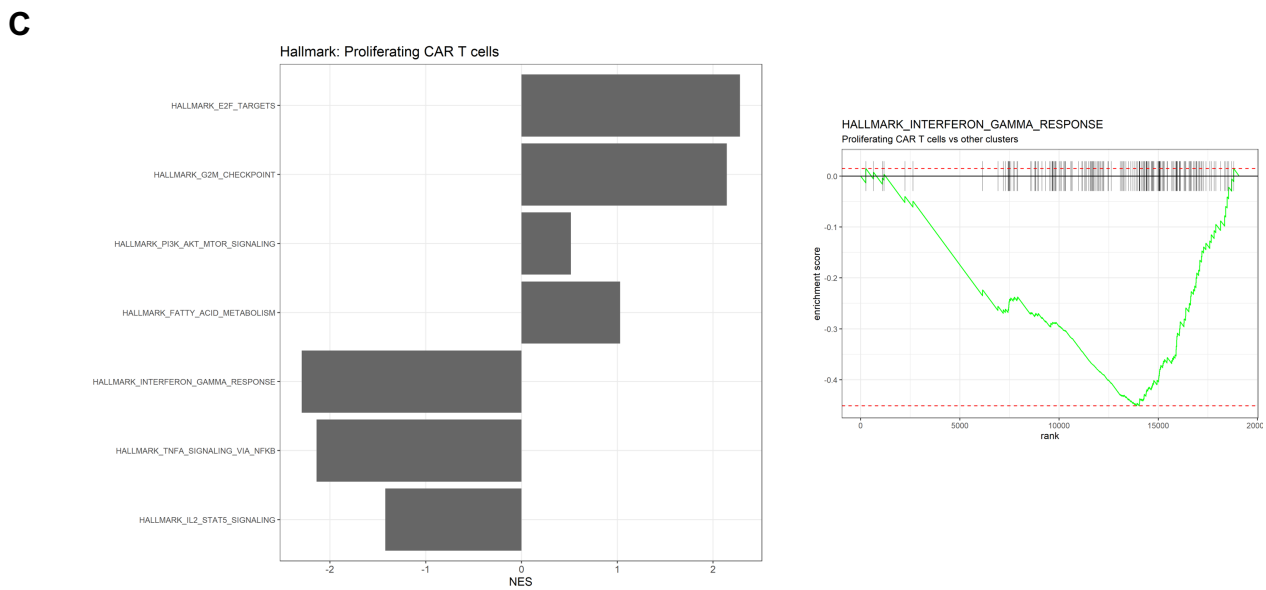

Supplementary Figure 5

Supplementary Figure S5. CAR-dependent stratification of intratumoral T-cell states in intracranial tumors

A. UMAP projections of tumor-infiltrating T cells across experimental conditions, including control CAR and individual CAR constructs, colored by transcriptionally defined T-cell states. Distinct populations corresponding to proliferative, metabolically stressed, highly activated/exhausted, regulatory, innate-like, and terminal cytotoxic effector T-cell states are resolved, with relative distributions varying across CAR designs.

B. Dot-plot visualization of state-defining marker genes across T-cell clusters, with dot size indicating the percentage of cells expressing each gene and color representing average expression, confirming transcriptional identities associated with proliferation, activation, exhaustion, metabolic stress, and effector differentiation.

C. Hallmark gene set enrichment analysis (GSEA) of proliferating CAR T-cell states, displayed as normalized enrichment scores (NES) for representative biological pathways. Moreover, a rtepresentative GSEA enrichment plot illustrating pathway enrichment in proliferating CAR T cells, demonstrating direction-dependent engagement of immune signaling programs. Collectively, these analyses reveal that CAR T-cell design shapes the distribution and transcriptional programs of intratumoral T-cell states within the CNS tumor microenvironment.

A

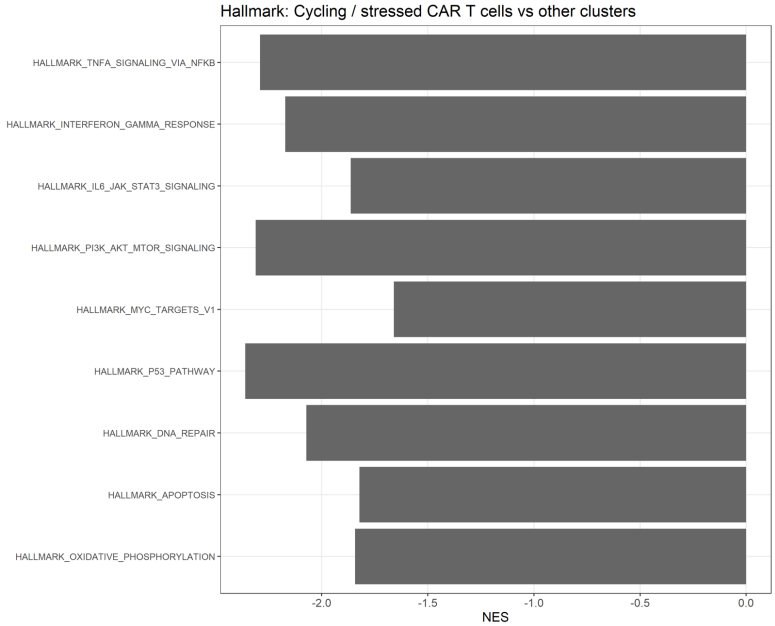

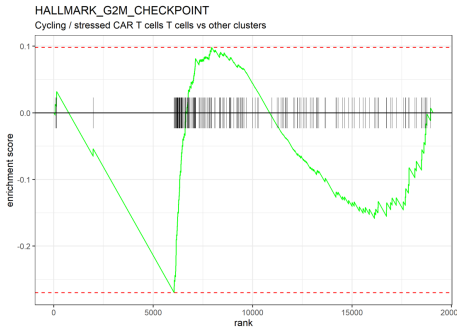

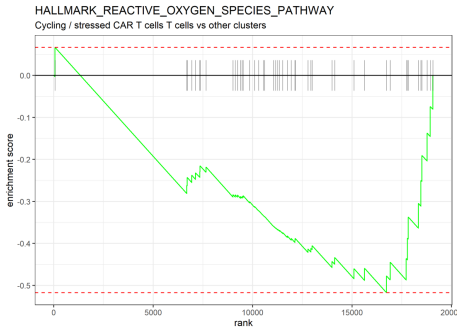

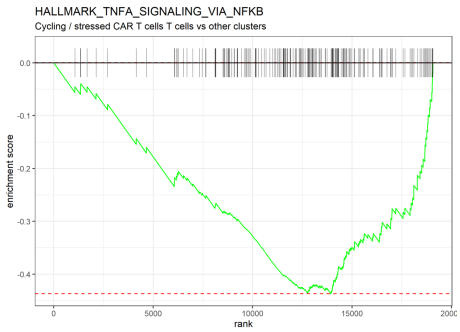

B

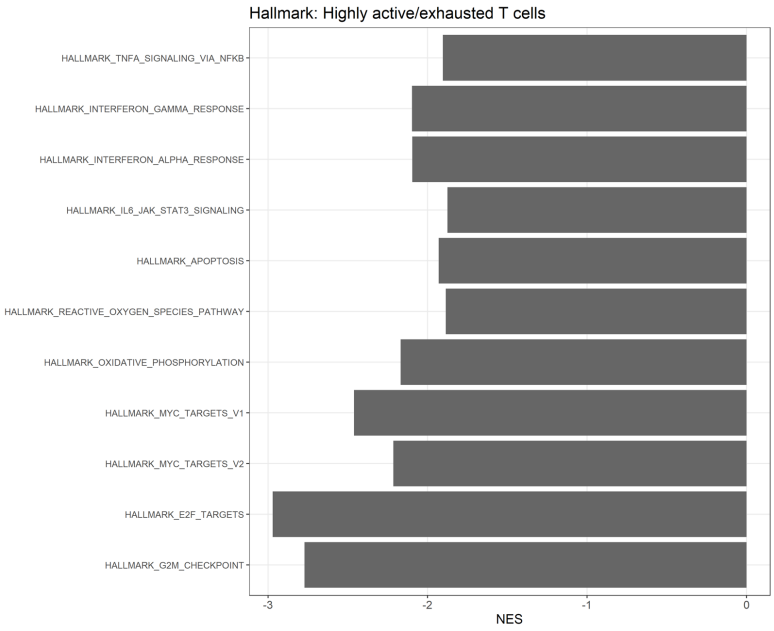

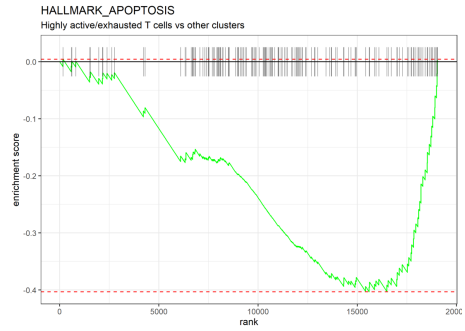

Supplementary Figure 6

Supplementary Figure S6: Distinct Hallmark pathway programs define cycling/stressed versus highly activated/exhausted CAR T-cell states.

A. Bar plot summarizing Hallmark gene set enrichment analysis (GSEA) comparing cycling/stressed CAR T cells with all other T-cell clusters. Bars represent normalized enrichment scores (NES) for selected pathways, indicating relative enrichment or depletion of cell-cycle, metabolic, stress-response, and inflammatory signaling programs. Representative GSEA enrichment plots are shown to illustrate direction-dependent pathway behavior in this state.

B. Bar plot summarizing Hallmark GSEA comparing highly activated/exhausted CAR T cells with all other T-cell clusters. NES values highlight engagement of inflammatory, activation-associated, apoptosis-related, and stress-linked transcriptional programs alongside relative attenuation of proliferative pathways. A representative GSEA enrichment plot for apoptosis is shown, illustrating direction-dependent enrichment characteristic of terminal or dysfunctional CAR T-cell states.

A

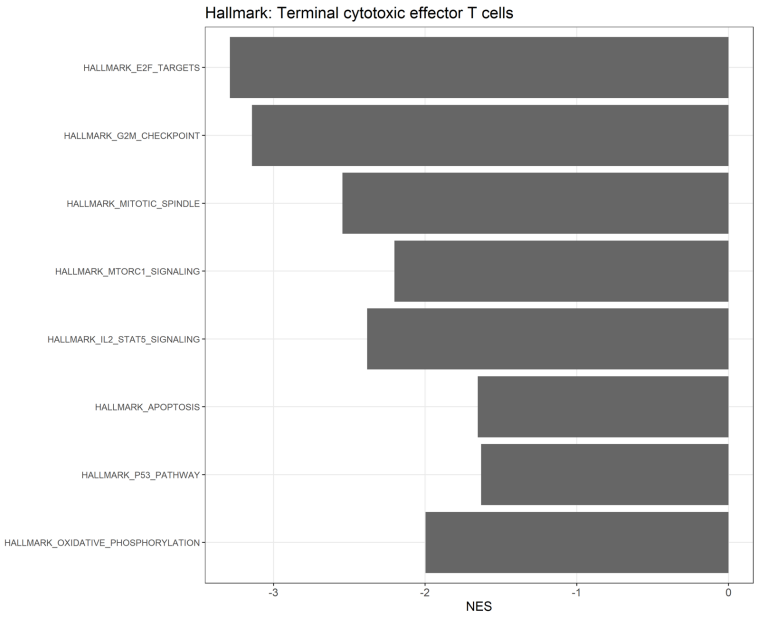

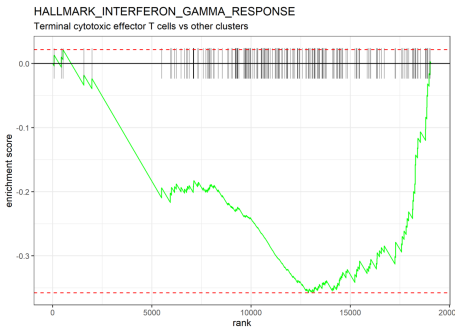

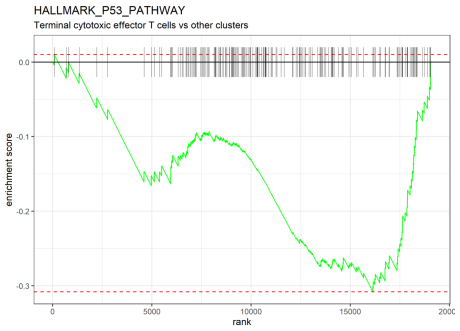

B

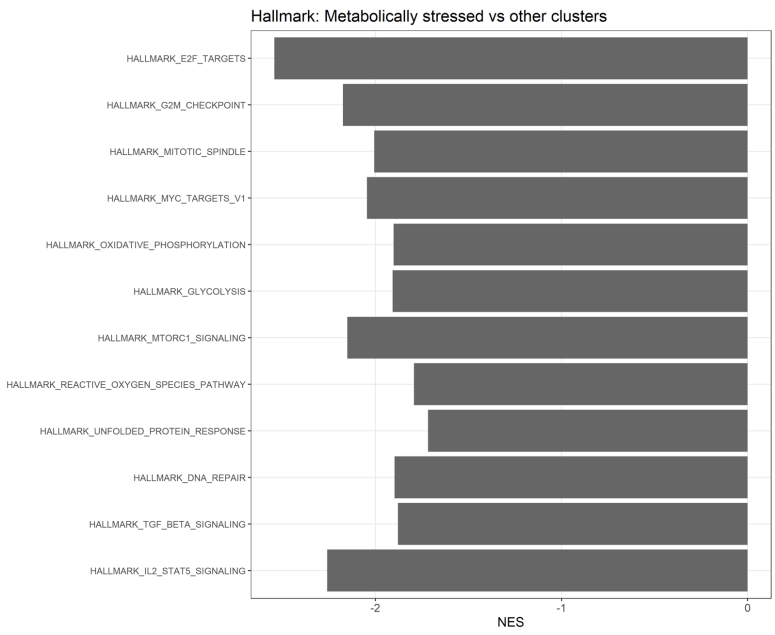

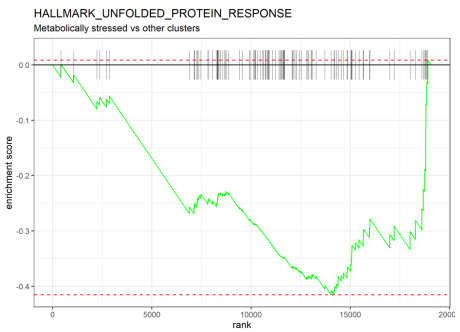

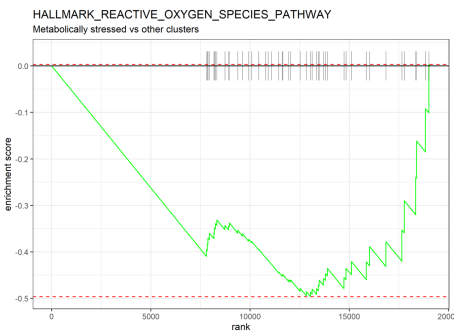

Supplementary Figure 7

Supplementary Figure S7. Hallmark pathway programs associated with terminal cytotoxic and metabolically stressed CAR T-cell states.

A. Bar plot summarizing Hallmark gene set enrichment analysis (GSEA) comparing terminal cytotoxic effector CAR T cells with all other T-cell clusters. Bars represent normalized enrichment scores (NES) for selected pathways, indicating relative depletion of inflammatory signaling, cell-cycle progression, and metabolic programs in terminal effector states. Representative GSEA enrichment plots for interferon gamma response and mTOR signaling are shown, illustrating direction-dependent attenuation of effector and survival-associated pathways in this state.

B. Bar plot summarizing Hallmark GSEA comparing metabolically stressed CAR T cells with all other clusters. NES values highlight enrichment of stress-response, unfolded protein response, and reactive oxygen species–associated pathways, alongside altered metabolic signaling. Representative GSEA enrichment plots illustrate transcriptional programs associated with metabolic and oxidative stress distinct from proliferative or terminal effector states.

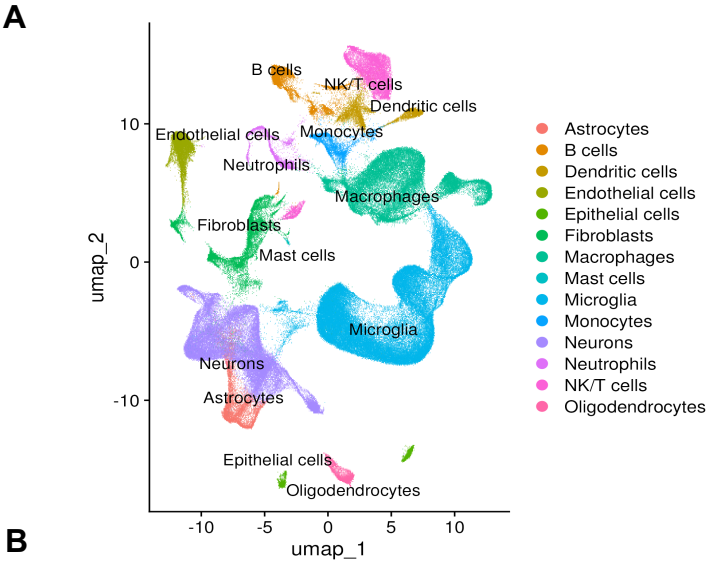

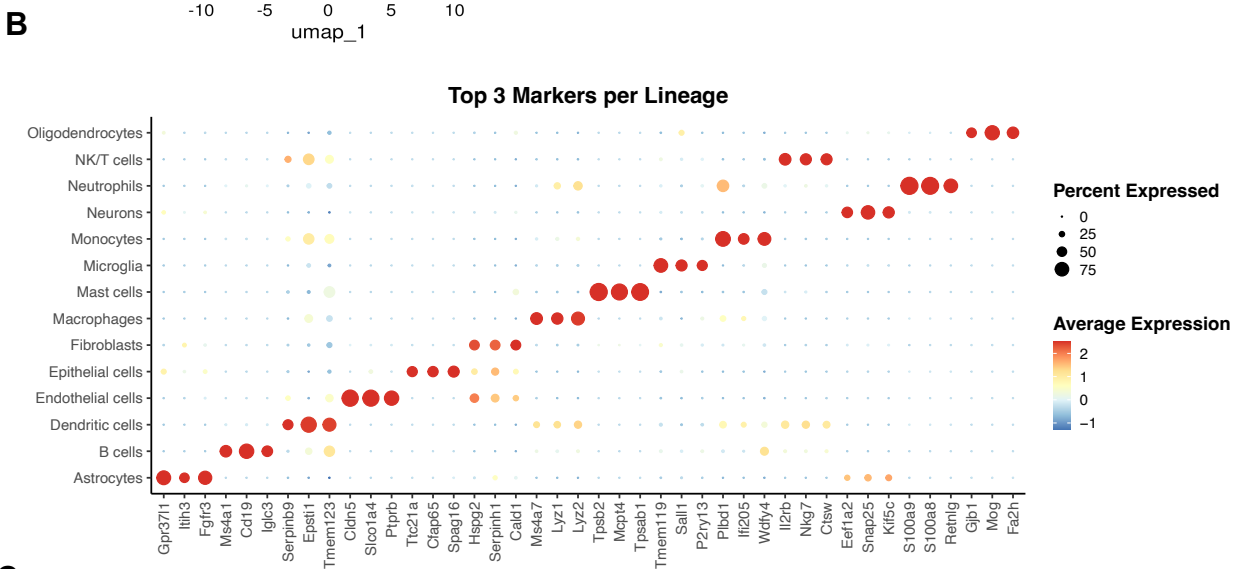

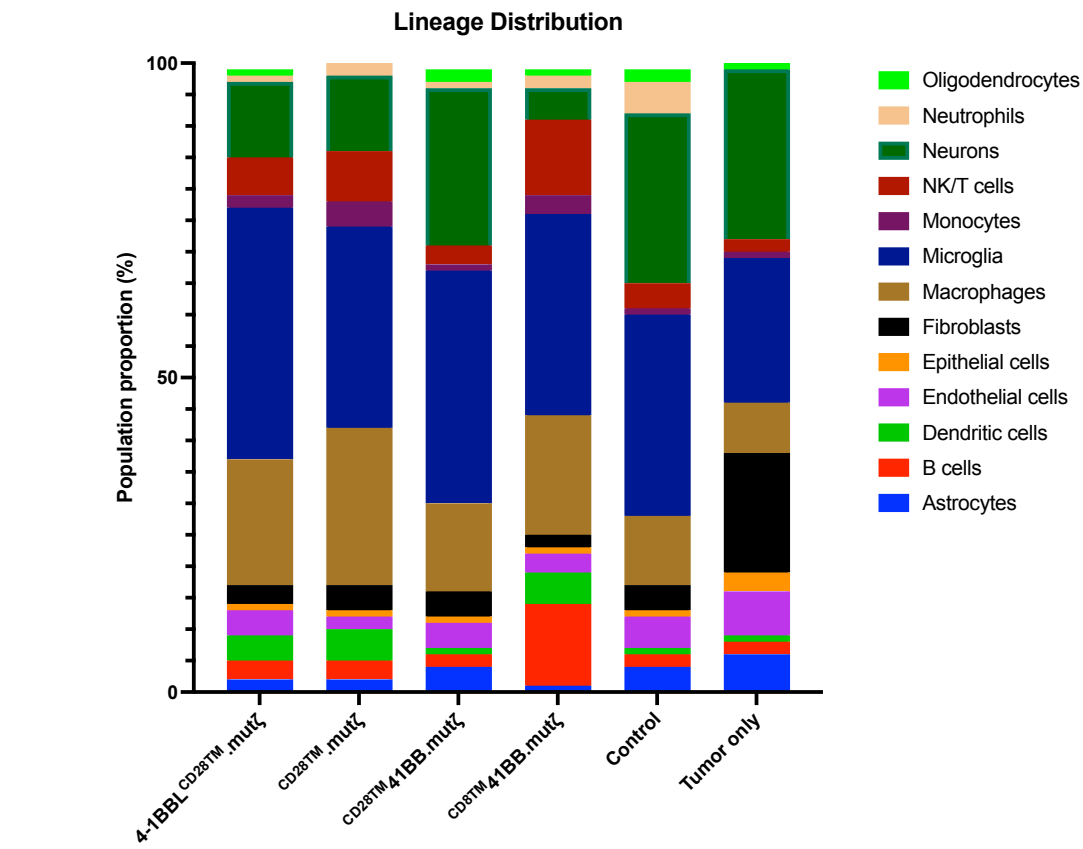

Supplementary Figure 8

Supplementary Figure S8: Global cellular composition and lineage annotation of the intracranial tumor microenvironment across treatment groups.

A. UMAP of integrated single-cell transcriptomes from pooled brain tumors, colored by major annotated lineages, demonstrating the diversity of immune, stromal, and neural-associated cell populations within the tumor microenvironment.

B. Dot plot showing the top three marker genes for each annotated lineage. Dot size indicates the proportion of cells expressing each gene, and color denotes scaled average expression, supporting lineage assignment across immune, stromal, and neural compartments.

C. Stacked bar plot showing the relative abundance of major cell lineages across the indicated treatment conditions. Each bar represents the proportional cellular composition of a pooled sample, highlighting treatment-associated shifts in the distribution of myeloid, lymphoid, stromal, and CNS-resident cell populations.

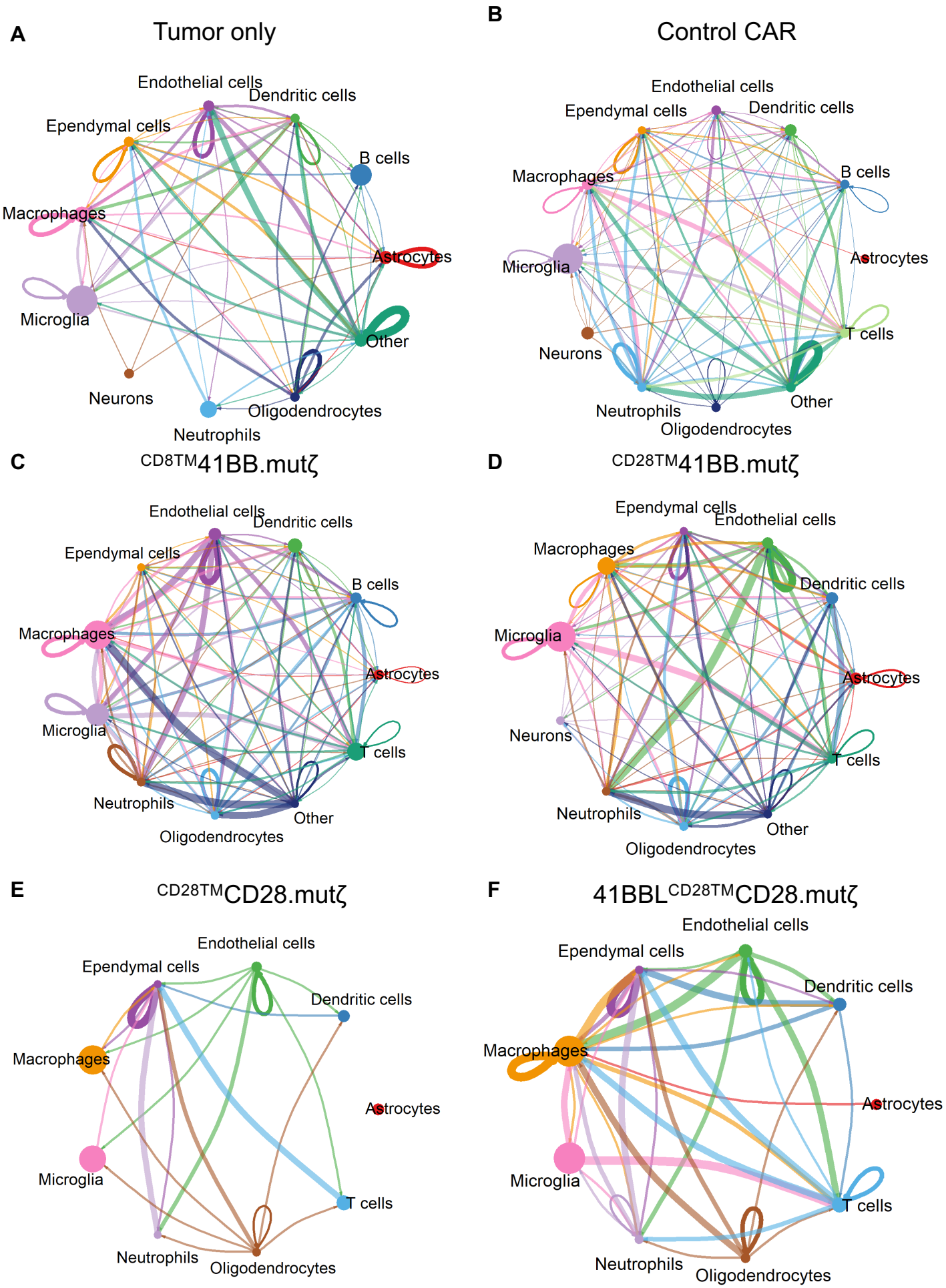

Supplementary Figure 9

Supplementary figure S9: CellChat analysis of intercellular communication networks in pooled brain tumors from immunocompetent mice treated with distinct B7-H3-directed CAR T-cell constructs.

A. Circular network plot showing inferred cell–cell communication across major tumor-associated populations in pooled samples from untreated mice. Nodes represent cell populations, and connecting edges represent predicted ligand–receptor interactions, with edge thickness proportional to interaction strength.

B. Circular network plot of inferred intercellular communication in pooled samples from mice treated with the control CD28TM–CD3ζ CAR construct.

C. Circular network plot of inferred intercellular communication in pooled samples from mice treated with the murine CD8TM-41BBCS-CD3ζ CAR construct.

D. Circular network plot of inferred intercellular communication in pooled samples from mice treated with the CD28TM-41BBCS-CD3ζ CAR,

E. Circular network plot of inferred intercellular communication in pooled samples from mice treated with the prototype CD28TM–CD3ζ CAR construct

F. Circular network plot of inferred intercellular communication in pooled samples from mice treated with the prototype 4-1BBL-CD28TM–CD3ζ CAR construct

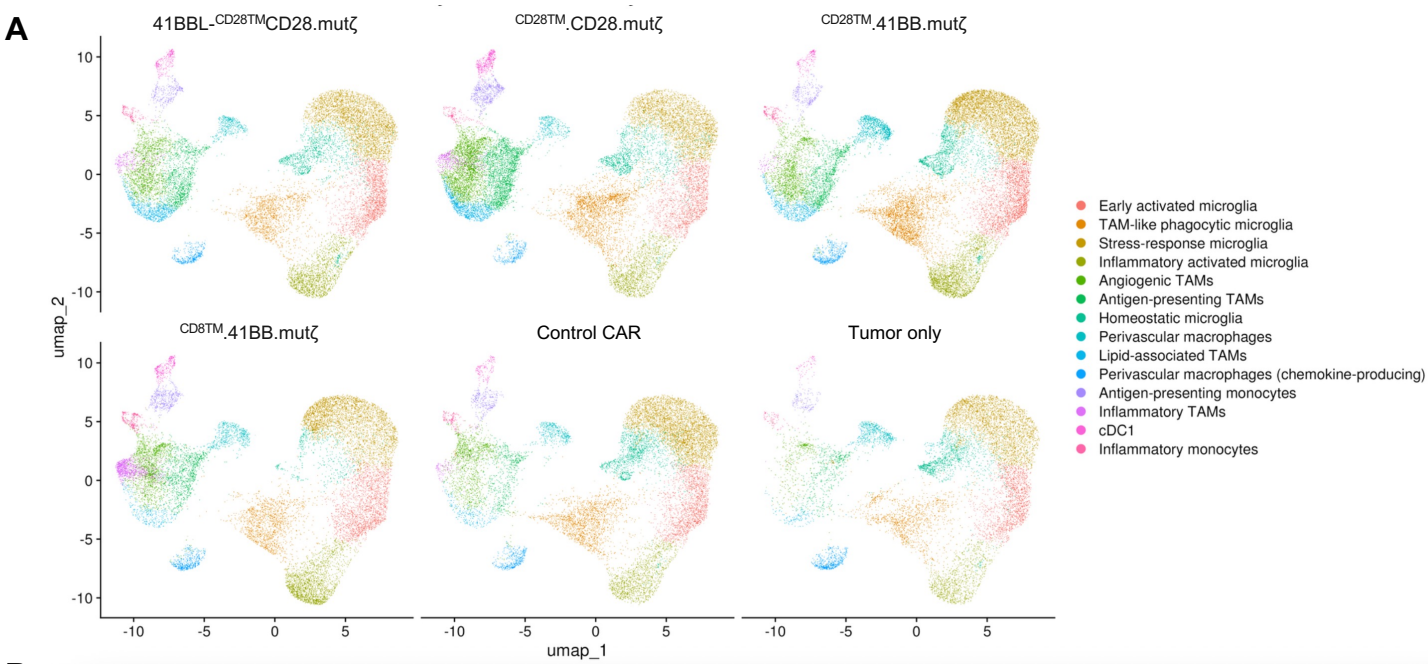

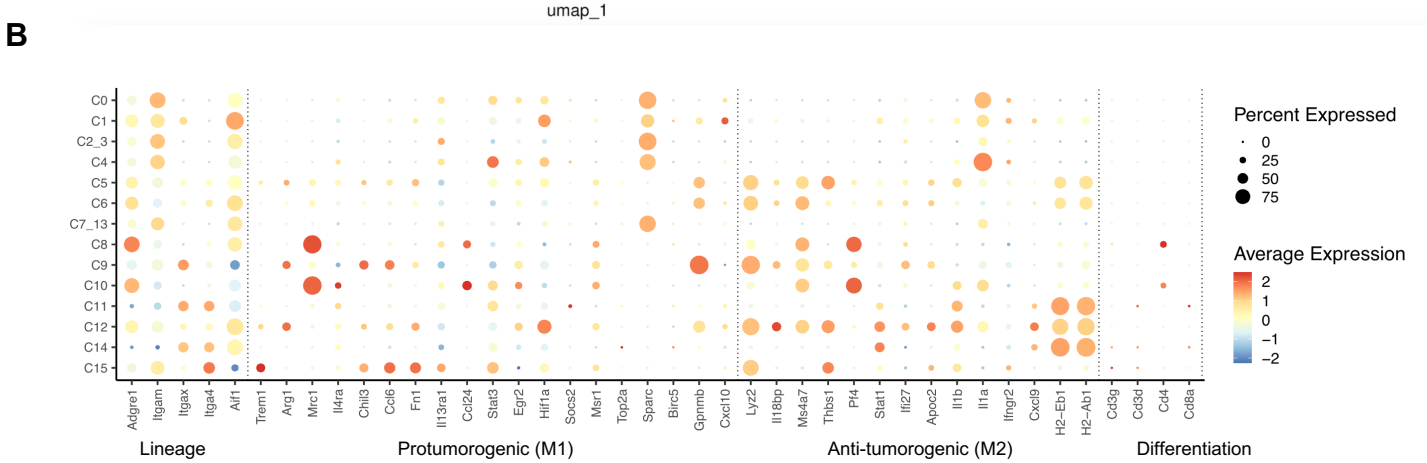

Supplementary Figure 10

Supplementary Figure S10: Myeloid lineage annotation and treatment-associated compositional shifts in the tumor microenvironment.

A. UMAP of integrated myeloid-lineage cells with differential spread across various treatment conditions

B. Dot plot of canonical marker genes across myeloid subclusters. Dot size indicates the percentage of cells expressing each gene, and color denotes scaled average expression, supporting cluster annotation.

C. Dot plot of curated functional gene programs across myeloid subclusters, including immunosuppressive, invasion-associated, recruitment, M1-like, and M2-like signatures, highlighting the functional heterogeneity of tumor-associated myeloid states.

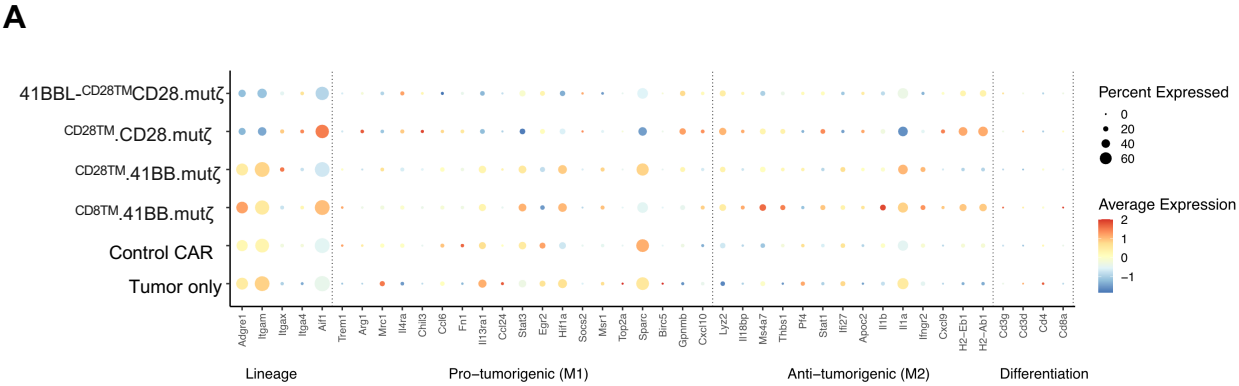

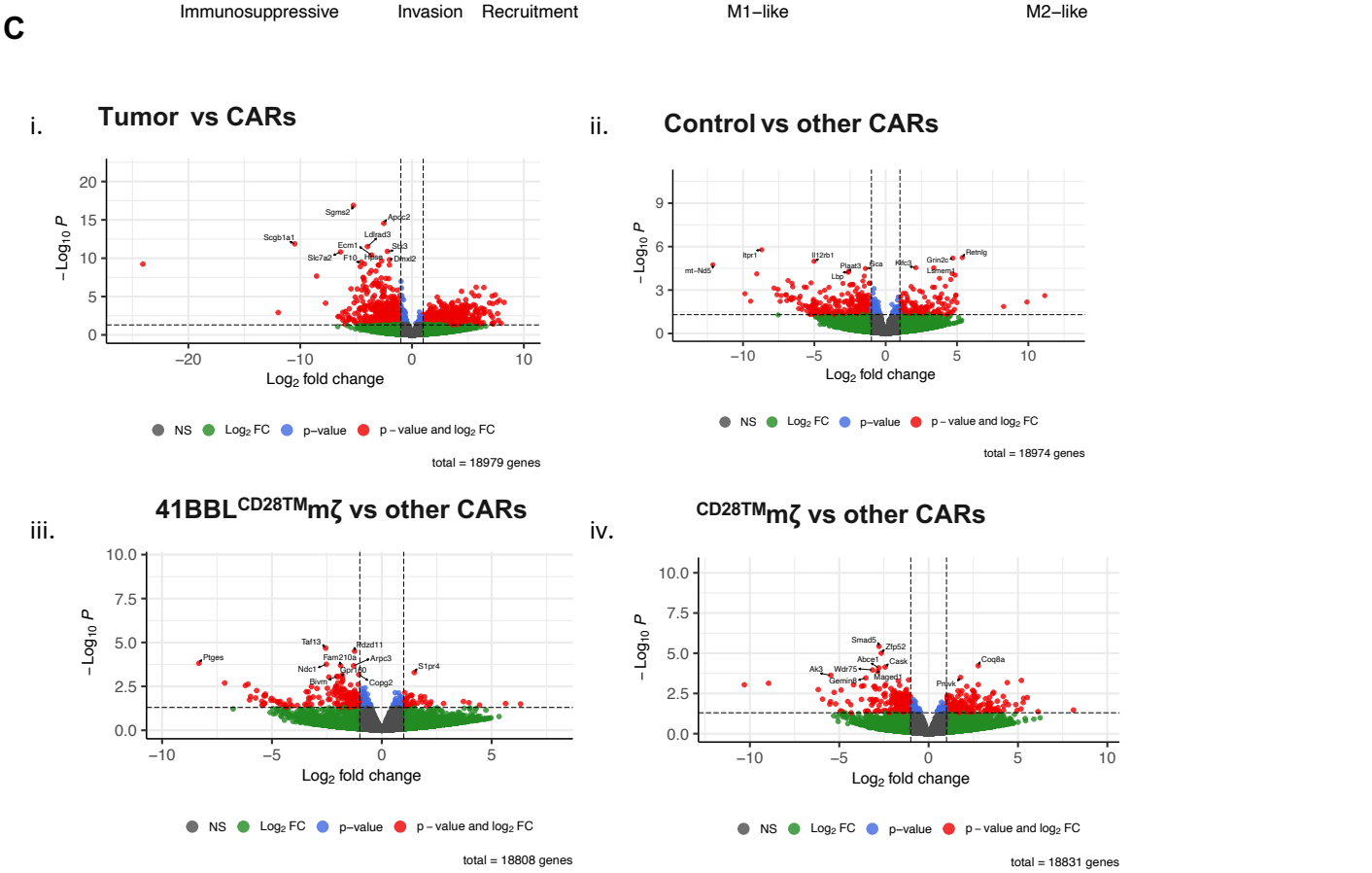

Supplementary Figure 11

Supplementary Figure S11: Myeloid polarization-associated gene expression across treatment conditions and myeloid subclusters.

A. Dot plot showing expression of lineage, pro-tumorigenic, anti-tumorigenic, and differentiation-associated genes across tumor-only and CAR-treated conditions. Rows represent treatment groups, including tumor only, control CAR, and distinct B7-H3-directed CAR constructs. Columns represent individual genes. Dot size indicates the percentage of cells expressing each gene, and color denotes scaled average expression, highlighting construct-dependent differences in myeloid transcriptional programming across treatment conditions.

B. Dot plot showing expression of curated functional gene programs across myeloid subclusters, including immunosuppressive, invasion-associated, recruitment, M1-like, and M2-like signatures, in tumor-only and CAR-treated samples. Dot size indicates the proportion of cells expressing each gene, and color represents scaled average expression. These data demonstrate that individual B7-H3 CAR designs are associated with distinct patterns of myeloid-state remodeling within the tumor microenvironment.

C. Differential gene expression (GSEA) data represented in volcano plots comparing tumor-only (i) , control (ii), CD28TM–CD3ζ (iii) and 4-1BBLCD28TM–CD3ζ (iv) CAR conditions against the remaining CAR groups, highlighting distinct treatment-associated transcriptional programs within the myeloid compartment.

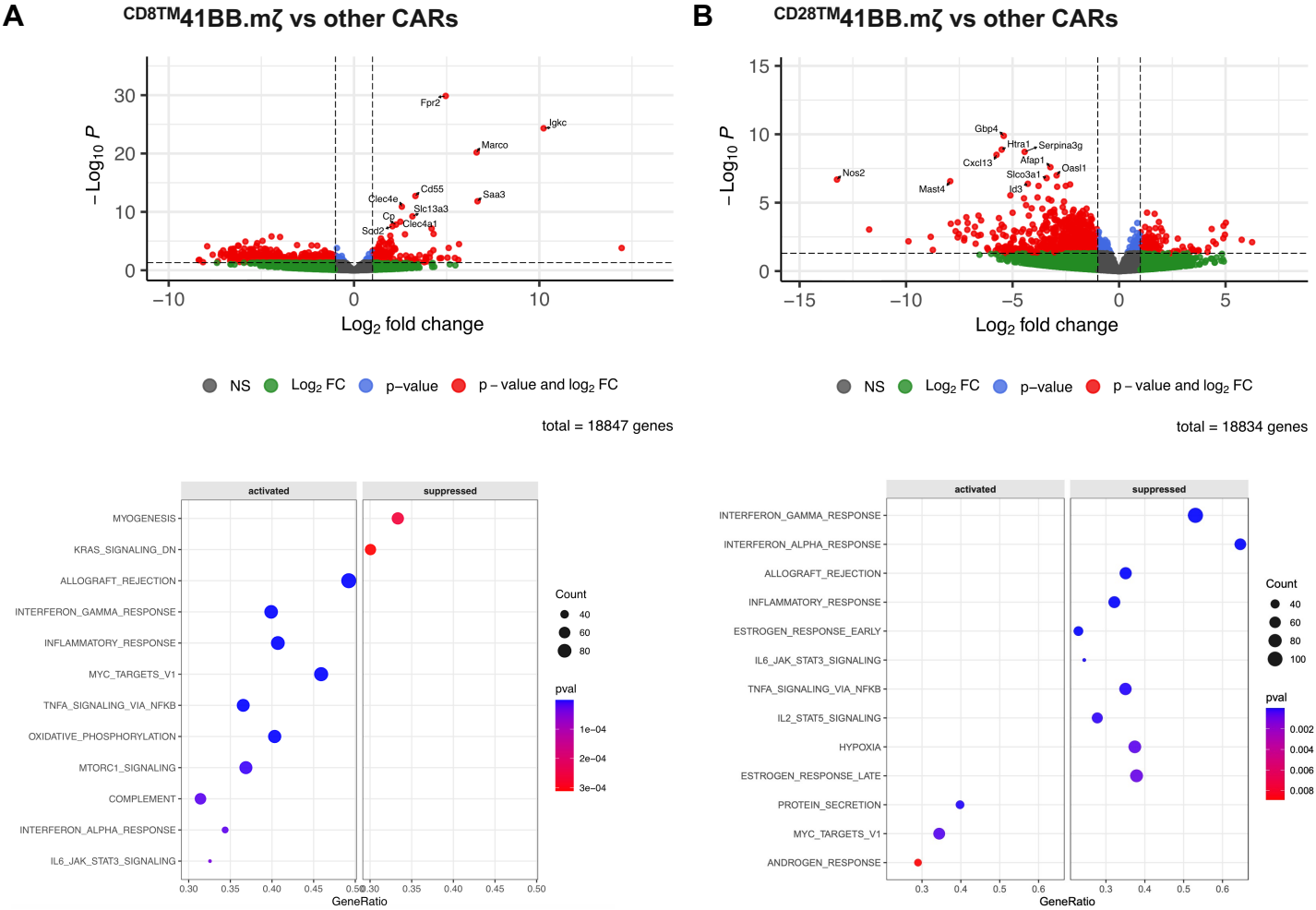

Supplementary Figure 12

Supplementary Figure S12. Construct-specific differential expression and pathway enrichment in CAR T cells

A. CD8TM-41BB.mζ CAR T cells versus all other CAR constructs. Volcano plot (top left) displays differential gene expression for CD8TM-41BB.mζ CAR T cells compared with all other CAR designs, plotted by $\log_2$ fold change and $-\log_{10}$ adjusted *p*-value, with significantly up- and down-regulated genes highlighted. The accompanying dot-plot (bottom left) summarizes pathway enrichment analysis based on differentially expressed genes, with dot size indicating the number of genes contributing to each pathway and color denoting statistical significance, illustrating transcriptional programs selectively associated with the CD8TM-41BB.mζ construct. Right panels: CD28TM-41BB.mζ CAR T cells versus all other CAR constructs.

B. Volcano plot (top right) shows differential gene expression for CD28TM-41BB.mζ CAR T cells relative to all other CAR designs, revealing a distinct construct-specific transcriptional profile. The corresponding dot-plot (bottom right) depicts pathway enrichment for genes differentially expressed in CD28TM-41BB.mζ CAR T cells, highlighting construct-associated engagement of immune signaling and cellular pathways distinct from those observed with other CAR architectures.

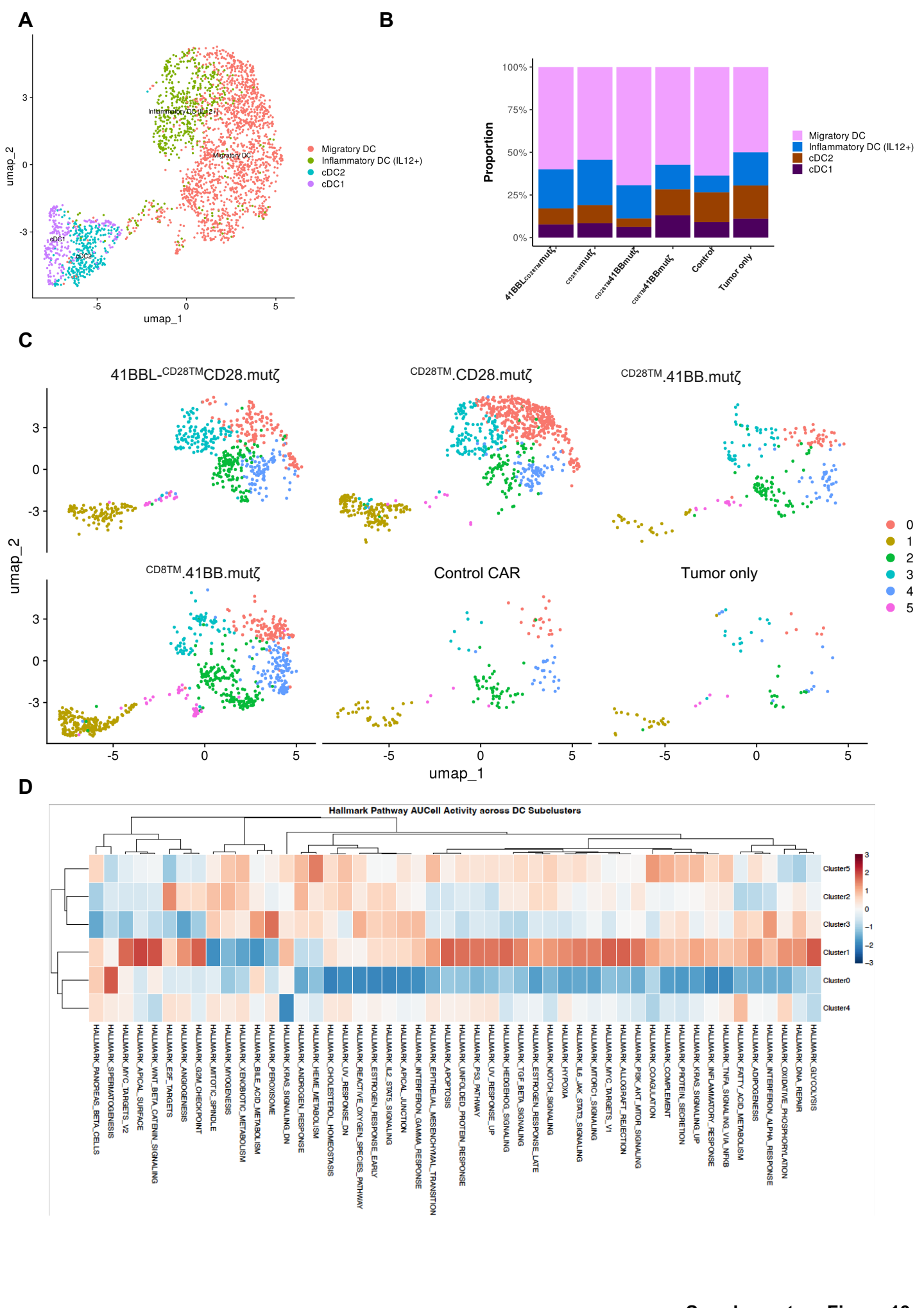

Supplementary Figure 13

Supplementary Figure S13. CAR-dependent remodeling of dendritic cell states within the intracranial tumor microenvironment

A. UMAP projection of intratumoral dendritic cells (DCs) identified from $CD45^+$ myeloid populations, colored by DC state. Distinct clusters corresponding to migratory dendritic cells, inflammatory IL-12–expressing DCs, DC1, and DC2 subsets are resolved, highlighting heterogeneity within the myeloid antigen-presenting compartment.

B. Stacked bar plot showing the proportional representation of annotated dendritic cell states across experimental conditions, illustrating treatment-associated shifts in DC composition following CAR T-cell therapy relative to control and tumor-only groups.

C. UMAP projections of dendritic cell states stratified by individual treatment conditions, including specific CAR constructs, control CAR, and tumor-only samples. These visualizations demonstrate construct-dependent restructuring of DC state distributions within the intracranial tumor microenvironment, with differential representation of inflammatory and migratory DC subsets across CAR designs.

D. Heatmap showing AUCell activity scores for Hallmark pathways across dendritic cell (DC) subclusters. Rows represent individual Hallmark gene sets, and columns represent DC subclusters (Cluster0–Cluster5). Color intensity reflects scaled AUCell scores (z-score), with blue indicating lower pathway activity and red indicating higher pathway activity relative to the mean (scale −3 to +3).

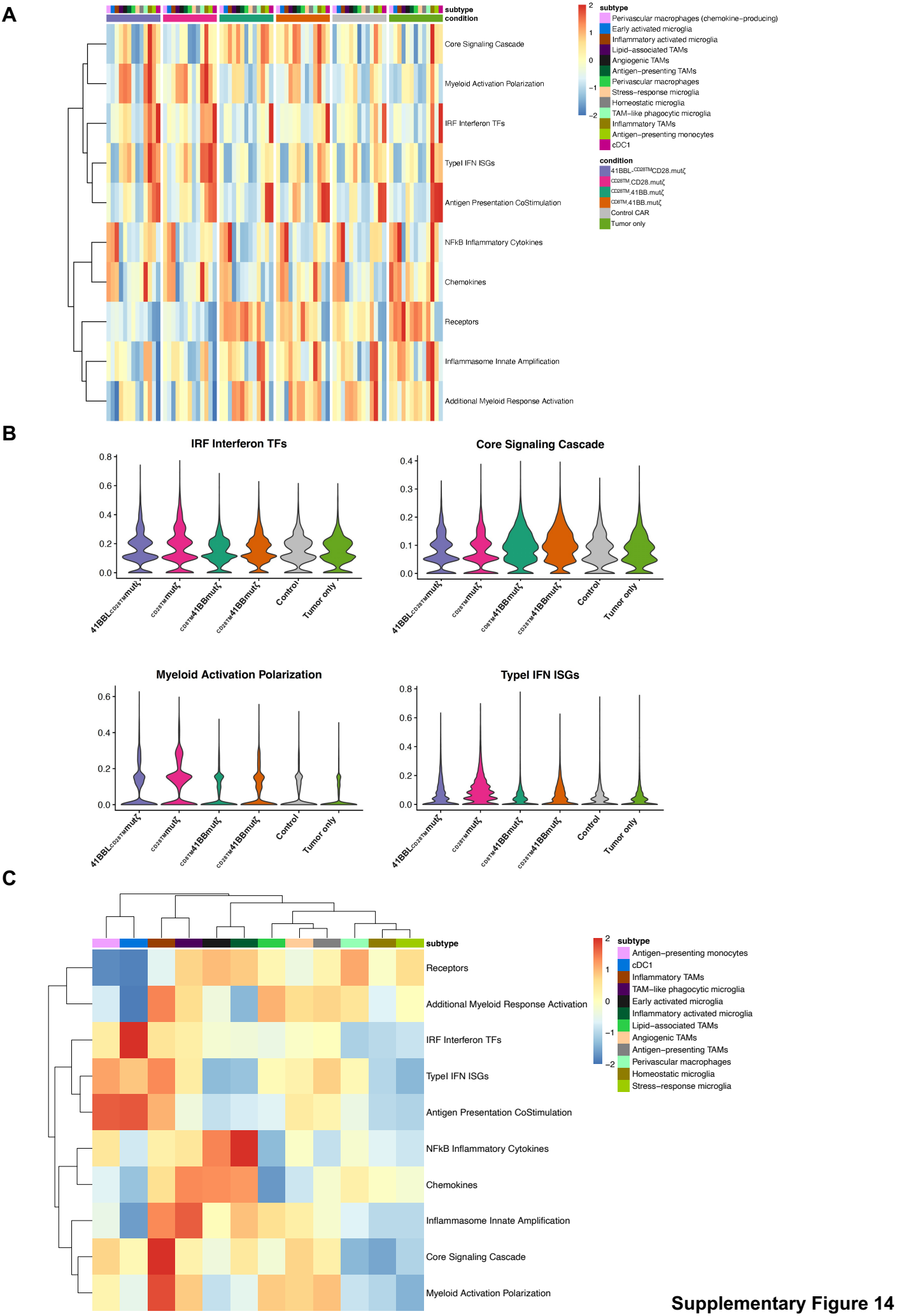

Supplementary Figure 14

Supplementary Figure S14: TLR7/8-associated transcriptional modules across tumor-associated myeloid subtypes and treatment conditions.

A. Heatmap showing scaled module scores for curated TLR7/8-associated transcriptional programs across individual myeloid subclusters, including pathways related to myeloid activation and polarization, type I interferon signaling, IRF/interferon-associated transcription factors, core signaling cascades, antigen-processing and costimulatory programs, NF-κB inflammatory cytokines, chemokines, receptors, interferon-induced amplification, and additional myeloid response modules. Columns represent subcluster-by-condition groupings, and rows represent functional gene modules.

B. Violin plots showing per-cell module score distributions for selected TLR7/8-related programs, including IRF/interferon-associated transcription factors, core signaling cascade, myeloid activation/polarization, and type I interferon interferon-stimulated genes, across tumor-only and CAR-treated conditions. These plots highlight condition-dependent differences in the magnitude and distribution of innate immune activation states within the myeloid compartment.

C. Heatmap summarizing relative module activity across myeloid subclusters for the same curated TLR7/8-associated programs. Color intensity denotes scaled enrichment, illustrating that TLR7/8-responsive signaling is not uniformly distributed across myeloid populations but is concentrated within specific inflammatory, antigen-presenting, and activated TAM or microglial states.

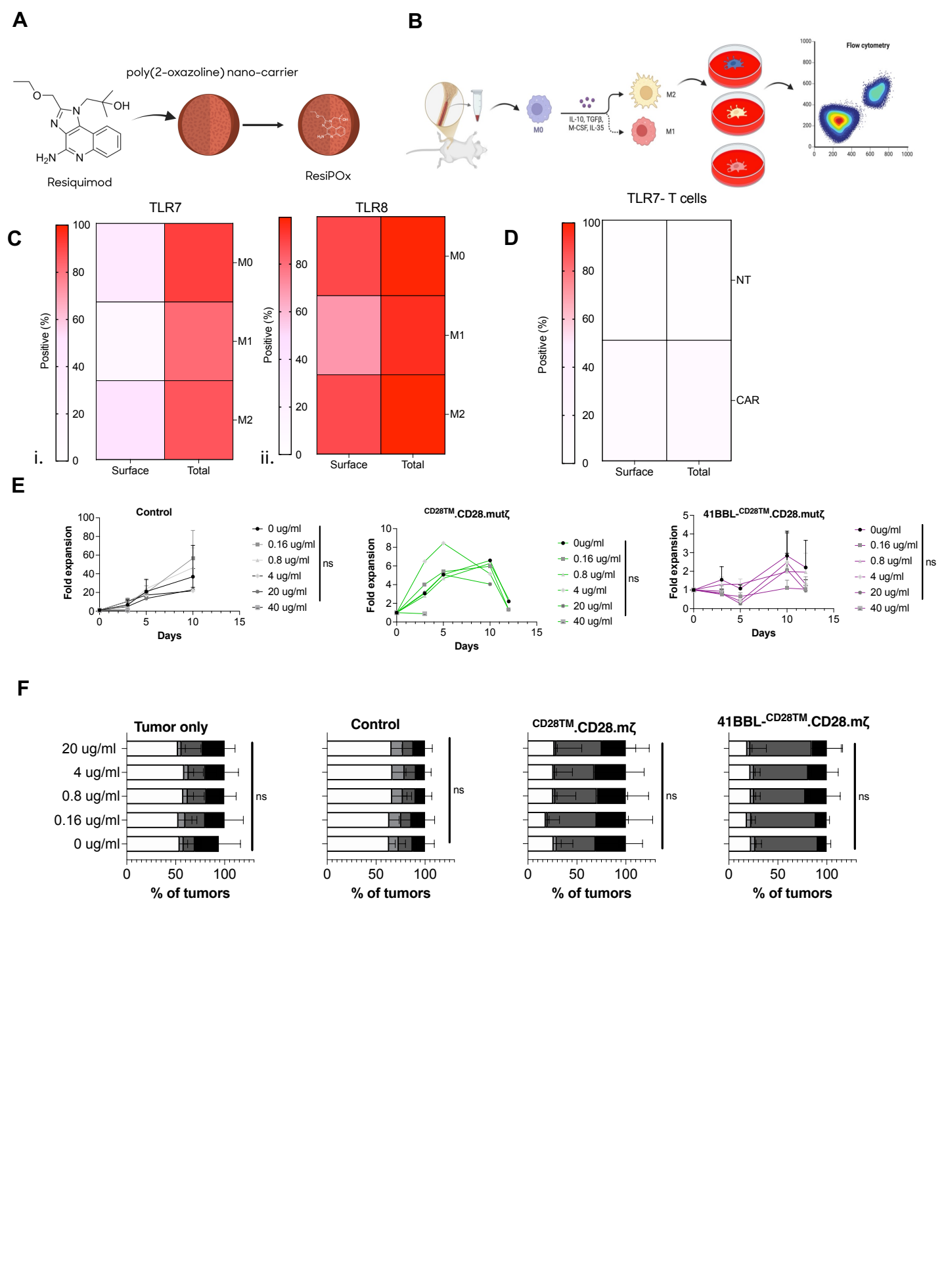

Supplementary Figure 15

Supplementary Figure S15: ResiPOx formulation, in vitro macrophage polarization, and immune-modulatory effects on CAR T-cell function.

A. Schematic of ResiPOx generation by encapsulating resiquimod within a poly(2-oxazoline) nanocarrier. *Created in BioRender. Yaacoub, S. (2026)* https://BioRender.com/dqo3f20

B. Experimental workflow for in vitro macrophage polarization, in which bone marrow-derived macrophages were driven toward M0, M1, or M2 states and subsequently analyzed by flow cytometry. *Created in BioRender. Yaacoub, S. (2026)* https://BioRender.com/f5gjgv5

C. Heatmaps summarizing relative expression of surface and intracellular TLR7 and 8 in BMDMs.

D. Heatmaps summarizing relative expression of surface and intracellular TLR7 in murine T cells.

E. Relative effects of ResiPOx on CAR T-cell expansion across an established concentration range. These data show the dose-dependent impact of ResiPOx exposure on CAR T-cell proliferative capacity, allowing assessment of concentrations that preserve T-cell fitness versus those associated with impaired expansion. There was no significant difference in expansion rates (ns)

F. Relative effects of ResiPOx on CAR T-cell cytotoxicity across the same established concentration range. These analyses quantify how ResiPOx influences CAR-mediated tumor cell killing as a function of dose and define the concentration window in which innate immune modulation can be achieved without substantially compromising CAR T-cell effector activity. There was no significant difference in cytotoxic capacity across concentrations (ns).

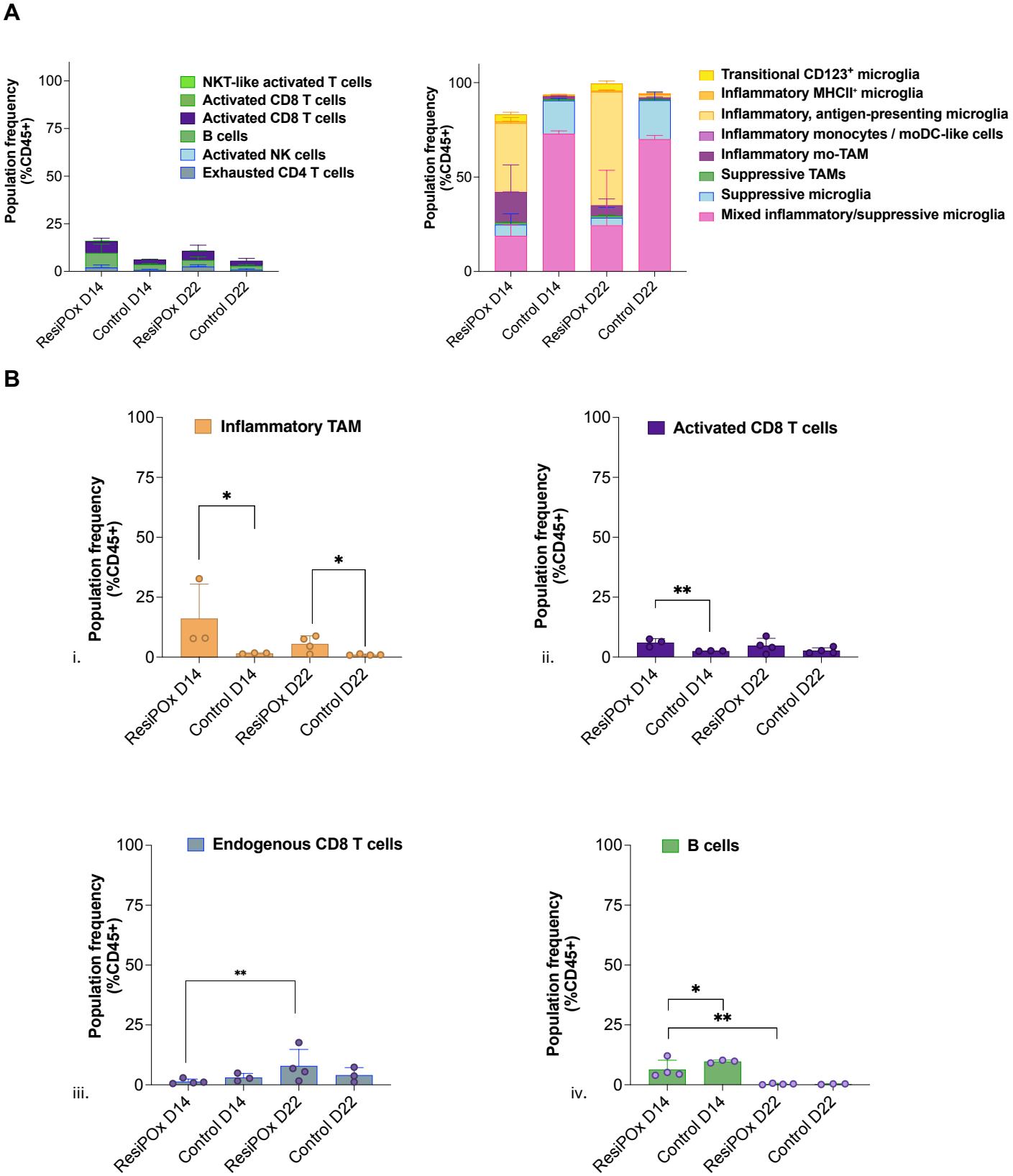

Supplementary Figure 16

Supplementary Figure S16: Flow cytometric characterization of immune remodeling induced by ResiPOx in the immunocompetent intracranial model.

A. Stacked bar plot summarizing the relative abundance of major T cell identified by flow cytometry across the indicated treatment groups, showing treatment-associated shifts in the composition of the tumor-infiltrating immune compartment (i). Stacked bar plot showing the distribution of marker-defined myeloid-dominant phenotypic subsets within the gated population of interest across treatment conditions, highlighting changes in activation-state composition after ResiPOx exposure (ii)

B. Quantification of inflammatory TAMs; ResiPOx induced a marked early change at day 4 relative to untreated tumors, with the largest separation observed at this time point, whereas values were reduced by day 12 but still greater relative to control (i). This pattern is consistent with an acute early response to innate immune stimulation followed by contraction at the later time point. Statistical significance is indicated as shown on the graph. Quantification of activated CD8 T cells (ii); this population showed early variation at day 4 but remained relatively stable across groups, suggesting that ResiPOx does not uniformly affect all tumor-infiltrating immune subsets. No major separation is visually apparent unless indicated by the statistical annotation. Quantification of endogenous CD8 T cells. This population trended upward at day 12 in treated tumors and was generally lower in untreated samples (iii). Quantification of B cells (iv); ResiPOx-treated tumors showed higher values at the earlier time point, followed by marked reduction by day 12 relative to control, indicating dynamic temporal remodeling of this compartment after treatment. The near-absent values in both groups at a later timepoint suggest a defined temporal pattern.

Data are shown as mean ± SEM with individual samples overlaid. Statistical comparisons were performed using one-way ANOVA followed by Tukey's multiple-comparisons test. Brains were harvested at day 4 or day 12 after ResiPOx administration; day 4 comparisons were made between untreated and ResiPOx-treated tumors, and day 12 comparisons were made between control and ResiPOx-treated tumors. *P < 0.05, **P < 0.01, ***P < 0.001, ****P < 0.0001.

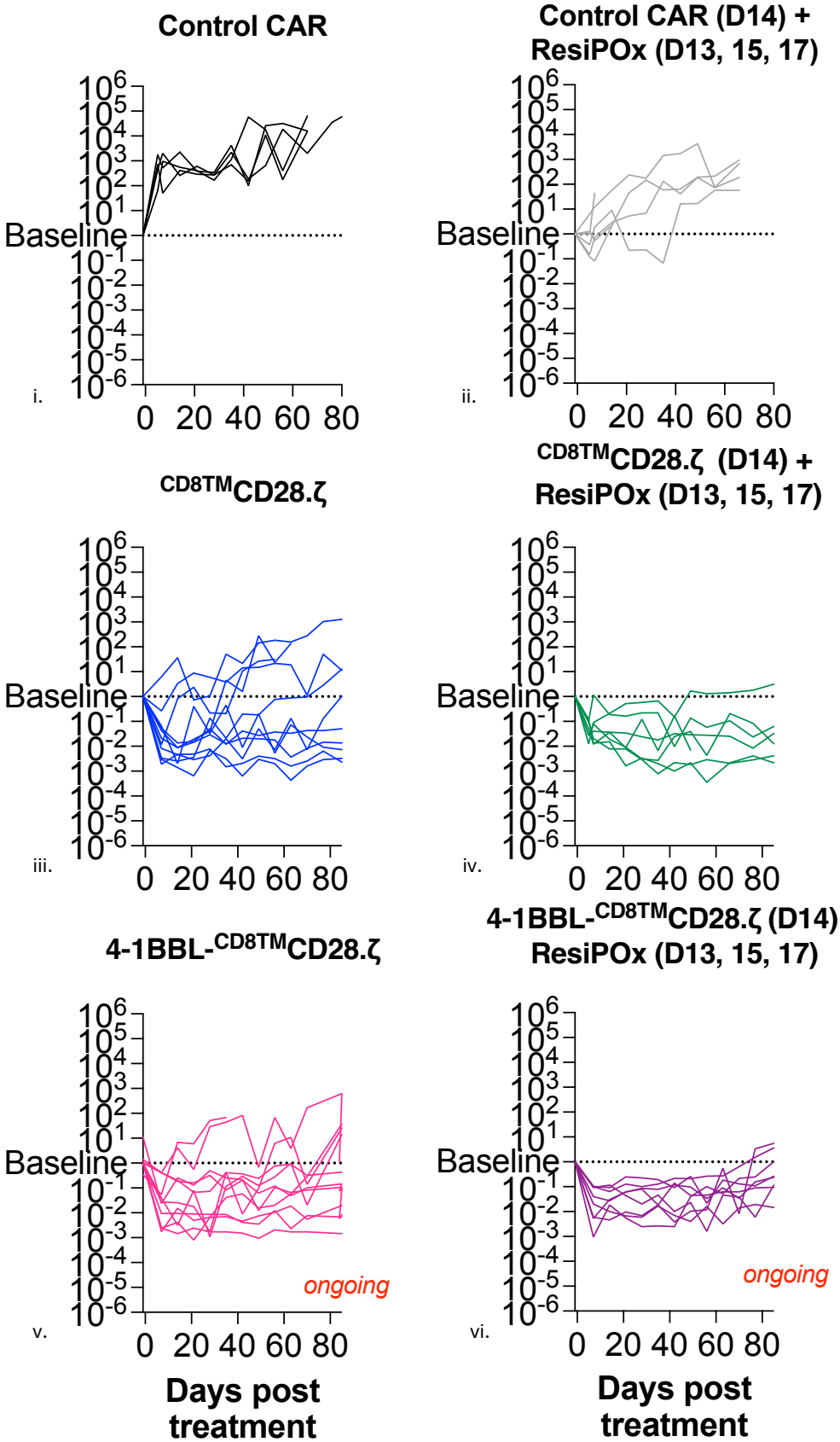

Supplementary Figure 17

Supplementary figure S17: Longitudinal bioluminescence kinetics of intracranial tumor burden across CAR T-cell treatment conditions.

i. Control CAR; Individual tumor growth trajectories demonstrate progressive increase in normalized flux over time.

ii. Control CAR + ResiPOx. Longitudinal flux curves show continued progression as well, reflecting slightly improved tumor response to adjunct resipox introduction.

iii. Functional CD8TM-harboring Human CAR exhibits intermediate suppression of bioluminescent signal, indicating variable therapeutic activity across the group.

iv. Functional CD8TM-harboring Human CAR with ResiPOX exhibits improved stable tumor burden control over time.

v. Functional 4-1BBL CD8TM-harboring Human CAR exhibits intermediate suppression of bioluminescent signal, indicating variable therapeutic activity across the group.

vi. Functional 4-1BBL CD8TM-harboring Human CAR with ResiPOX exhibits improved stable tumor burden control over time.

Normalized total flux is shown over time for individual mice in each treatment group, with each line representing a single animal. Bioluminescent signal was normalized to baseline to enable comparison of relative tumor progression kinetics across conditions. D556-ffluc-ridden NSG mice were treated at day 14 and respective resipox regimens (D13, 15, 17) accordingly .

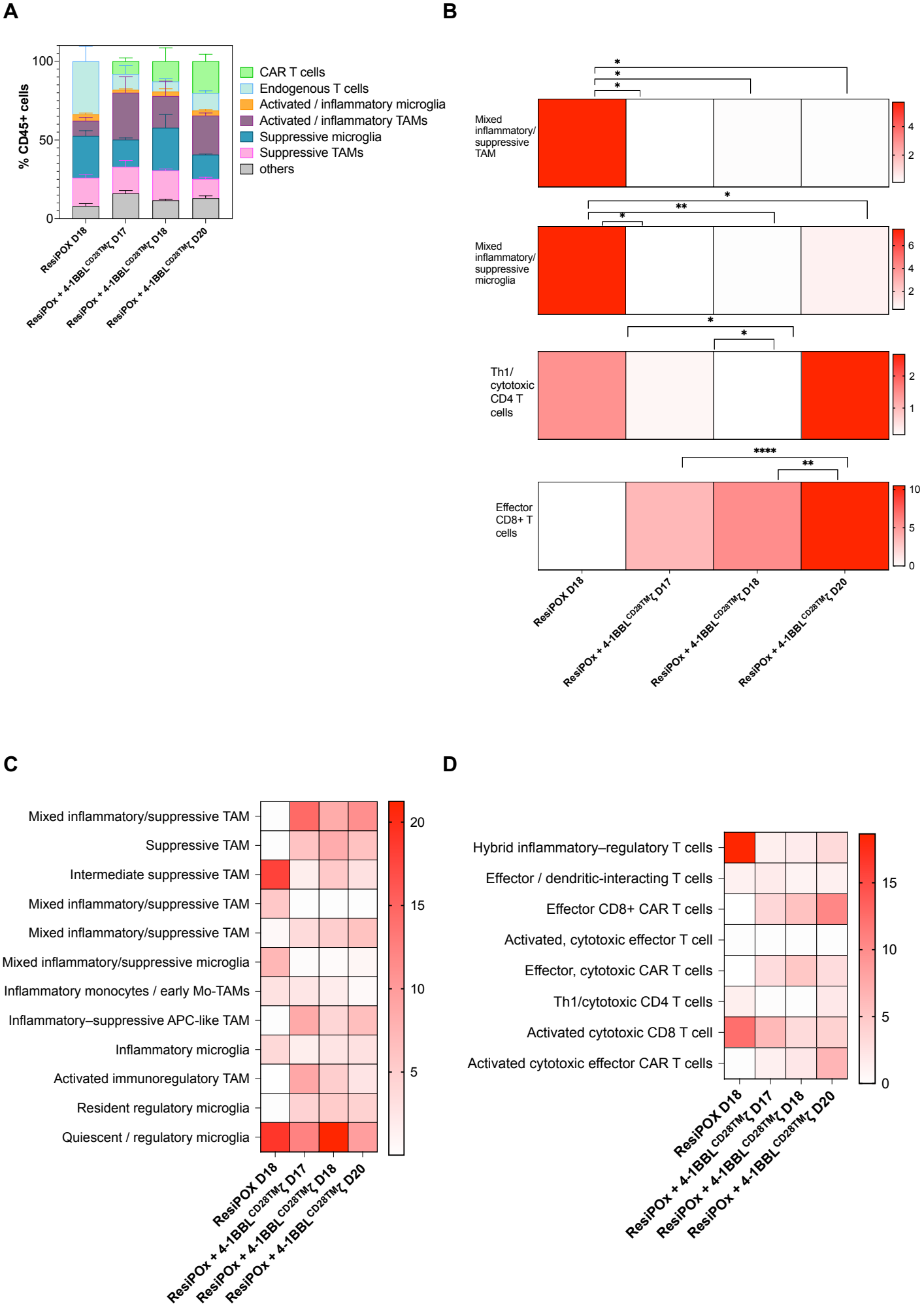

Supplementary Figure 18

Supplementary Figure S18: Time-dependent remodeling of myeloid and T-cell states following ResiPOx alone or ResiPOx plus 4-1BBL CAR T-cell therapy in the immunocompetent intracranial model.

A. Schematic overview of the analytic comparison strategy. Brain tumors were harvested at defined time points after treatment with ResiPOx alone or ResiPOx combined with 4-1BBL CAR T cells, and lineage/subcluster frequencies were compared to define early temporal changes in the tumor immune microenvironment.

B. Heatmaps showing relative abundance of selected immune states across treatment-time conditions. Columns represent ResiPOx/ ResiPOx + 4-1BBL CARs with samples harvested at either day 17, 18, and 20. Rows show the indicated populations: mixed inflammatory/suppressive TAMs, mixed inflammatory/suppressive microglia, Th1/cytotoxic CD4 T cells, and effector CD8-positive T cells. Color intensity reflects relative enrichment of each population. Statistical annotations above the heatmaps indicate significant pairwise differences across time points and treatment conditions, supporting dynamic restructuring of both myeloid and lymphoid compartments after innate immune stimulation and combination therapy.

C. Heatmap of treatment-time-associated changes across myeloid subclusters. Rows represent distinct macrophage and microglial states, including suppressive TAMs, intermediate suppressive TAMs, mixed inflammatory/suppressive TAMs, mixed inflammatory/suppressive microglia, inflammatory monocyte-derived TAMs, inflammatory–suppressive APC-like TAMs, inflammatory microglia, activated immunoregulatory TAMs, resident regulatory microglia, and quiescent/regulatory microglia. Columns correspond to the same treatment-time conditions shown in panel B. These data indicate marked temporal heterogeneity in myeloid-state representation, with selective enrichment of inflammatory, suppressive, and regulatory programs depending on treatment context and harvest timing.

D. Heatmap of treatment-time-associated changes across T-cell subclusters. Rows represent hybrid inflammatory–regulatory T cells, effector/dendritic-interacting T cells, effector CD8-positive CAR T cells, activated cytotoxic effector T cells, effector cytotoxic CAR T cells, Th1/cytotoxic CD4 T cells, activated cytotoxic CD8 T cells, and activated cytotoxic effector CAR T cells. Columns represent ResiPOx day 18, ResiPOx + 4-1BBL CAR day 17, ResiPOx + 4-1BBL CAR day 18, and ResiPOx + 4-1BBL CAR day 20. Color intensity denotes relative abundance. Together, these findings show that combination treatment is associated with time-dependent accumulation of activated cytotoxic T-cell states alongside coordinated remodeling of tumor-associated myeloid populations.